On the Validity and Limitations of 1D Model for Heat and Mass Transfer Performance Evaluation in a Multilayer Binder-Free Desiccant Dehumidifier: Isothermal Dehumidification with Internal Cooling

Jubair A. Shamim[1*], Easwaran Krishnan[1], Mingkan Zhang[1], Lei Gao[1], Kai Li[1], Wei-Lun Hsu[2], Hirofumi Daiguji[2], Kashif Nawaz[1*]

[1]Building Technologies Research Integration Center, Building and Transportation Science Division, Oak Ridge National Laboratory, 1 Bethel Valley Road, Oak Ridge, TN 37830, USA

[2]Department of Mechanical Engineering, The University of Tokyo, 7-3-1 Hongo, Bunkyo-Ku, Tokyo 113-8656, Japan

[*]Corresponding authors' email:

shamimja@ornl.gov; nawazk@ornl.gov

Abstract

Efficient humidity control is essential for maintaining indoor thermal comfort, yet conventional vapor-compression-based dehumidifiers are energy-intensive. Employing separate sensible and latent cooling through desiccant-coated heat exchangers (DCHEs) combined with evaporative coolers offers energy savings of up to 80% compared to conventional systems. However, the dehumidification performance of DCHEs remains limited due to the use of polymer binders for coating desiccant materials onto heat exchange surfaces. In our previous study, we developed a multilayer fixed-bed binder-free desiccant dehumidifier (MFBDD) that demonstrated high dehumidification capacity and low pressure drop compared to rotary desiccant wheels. Nevertheless, its potential for further enhancement through internal cooling and the use of step-shaped adsorption isotherms has not been explored. In this study, a physics-based one-dimensional (1D) transient model is developed and validated to capture the coupled heat and mass transfer processes in the MFBDD and extended to simulate internal cooling using a high-capacity composite metal–organic framework, MIL-101/GO-6 (water uptake ≈1.6 g/g within 35–47% RH). The model enables detailed analysis of local air and bed temperature dynamics and quantifies how internal cooling affects the dehumidification performance under a wide range of operating conditions. Results show that integrating internal cooling and using MIL-101/GO-6 enhance mass adsorbed, moisture removal capacity, and dehumidification effectiveness by 50%–99% compared with the M.S. Gel baseline. The study further reveals that achieving near-isothermal operation requires simultaneous enhancement of the convective heat transfer coefficient and heat exchange surface area. This work provides the first detailed physical insight into the interplay between internal cooling and step-shaped isotherms in a binder-free desiccant device and establishes a validated modeling framework for scaling up and system-level performance evaluation of next-generation energy-efficient dehumidification systems.

Keywords: multilayer binder-free desiccant dehumidifier; one-dimensional model; integrated internal cooling; step-shape isotherm; heat and mass transfer; isothermal dehumidification

1 Introduction

As buildings serve as the primary environment for work and living, people spend approximately 90% of their time indoors [1]. Therefore, controlling indoor humidity is essential to safeguard occupant well-being and prevent sick building syndromes. Elevated humidity level may result in mold growth, bacterial proliferation, and other moisture-related issues, while excessively low humidity can lead to respiratory discomfort and various health related problems [2]. Conventional indoor humidity control relies on energy-intensive vapor compression systems, which cool air below its dew point to condense moisture, followed by reheating to achieve ideal indoor temperatures [3]. In contrast, desiccant-based hybrid air-conditioners (DHAC) dehumidify air above the dew point using suitable desiccant materials and are often paired with evaporative coolers to achieve desired indoor temperatures for occupants' thermal comfort [4, 5]. This approach separates sensible and latent load management, offering a more energy-efficient solution [6]. Studies have shown that DHAC has the potential to reduce electricity consumption by 30%–80% [7-9] and achieve 75%-120% higher second law efficiency [10] as compared to conventional vapor compression-based systems. Besides DHAC, desiccant materials are also attractive for drying applications due to their low energy consumptions [11].

DHAC can be designed either using solid desiccant [12, 13] or liquid desiccant dehumidifier [14]. However, solid desiccant systems (SDS) are less prone to corrosion and have no desiccant leakage issue when compared to liquid ones [15]. Therefore, significant efforts have been devoted to evaluate the performance of SDS using a variety of desiccant materials. To date, silica gel or silica gel-based composites are the most widely used desiccants as they are cheap and easy to synthesize in large scale. However, several other new desiccants with large water vapor uptake capacities and improved thermophysical properties have been investigated too, including metal-organic frameworks (MOFs) [13, 16-18], super adsorbent polymers (SAPs) [19, 20], and hydrogels [21, 22]. Among these new desiccants, MOFs have attracted growing attention owing to their unique porous architectures and facile functionalization, which make them promising candidates for applications in moisture control [5, 6] heat transformation [23-27], and HVAC [28, 29]. In particular, MOFs exhibit great potential for dehumidification applications due to their tunable step-shaped sorption isotherms, which enable high moisture uptake within a narrow relative humidity range, allowing performance optimization for specific climate conditions [30-32]. Studies have demonstrated that MOF-based desiccants or composites can outperform silica gel and zeolite-based desiccants by 30%–50% in terms of dehumidification capacity [16].

In addition to the development of new desiccant materials, innovative designs of solid desiccant systems (SDS) have also been explored, including desiccant-coated heat exchangers (DCHEs) [33], rotary desiccant wheels [34, 35], packed bed systems [36, 37] and fluidized bed systems [38]. Nevertheless, DCHEs offer distinct advantages over other system configurations, including the absence of moving parts, minimal size constraints, high surface-area-to-volume ratios, reduced pressure drop, and the potential for internal cooling arrangements. Consequently, multiple studies have evaluated the moisture removal performance of DCHEs using a variety of desiccant materials and geometric configurations of the heat exchanger substrate [23, 24, 39-43]. However, since adsorption is an exothermic process, the enthalpy released during water vapor uptake increases the desiccant bed temperature, thereby reducing dehumidification performance. Suppressing this temperature rise is therefore crucial for enhancing moisture removal efficiency. Li et al. [25] reported that higher face velocities and lower bed temperatures are instrumental in improving mass transfer coefficients in SDS. In this context, DCHEs are particularly attractive, as internal cooling can be readily integrated into their design to mitigate temperature rise during

adsorption [29, 43-45]. **Table 1** summarizes some of the recent studies that have investigated the performance of internally cooled DCHEs.

Table 1. Summary of the recent studies investigated the performance of internally cooled DCHEs.

Ref.	Methodology/ Publication Year	Desiccants Used	Key Conclusions and Critique/Research Gaps
[10]	Steady state thermodynamic model (1st and 2nd law analysis) (2020)	Ceramic silica gel, PVA-LiCl (50w%), SAP-HCO_2K (50w%), SAP-LiCl (50w%)	▪ Composite desiccants exhibited 2.6 times higher 2nd law efficiency and four times higher dehumidification capacity as compared to silica gel. ▪ Reducing hot water temperature by 10 ℃ achieved two times higher 2nd law efficiency. But it will also adversely affect the moisture removal ability. Hence a tradeoff is required. ▪ Chilled water flowrate was constant at 2.5-2.7 L/min. Thus, the article investigated only the influence of varying chilled water temperatures. ▪ Despite four desiccants being used, the article did not report the adsorption-desorption isotherms of the desiccants.
[46]	Modeling (2018)	Silica gel paper composite, Aluminum fumarate	▪ The study reported a step-shape adsorption isotherm of aluminum fumarate, but the maximum uptake was limited to 0.5 g/g only. ▪ Although the study compared adiabatic and water-cooled cases, the study did not investigate the influence of varying chilled water temperature and mass flow rates. ▪ Water cooled cases outperformed the adiabatic cases and achieved 70% higher removal of adsorbate. ▪ Although water uptake capacity of silica gel was lower, it achieved 17% and 66.6% higher adsorbate removal for water cooled and adiabatic cases, respectively, when compared to aluminum fumarate. The authors did not explain the underlying reasons for high performance of silica gel.
[47]	Modeling & Experiment (2021)	Type B silica gel with epoxy-polyester binder	▪ The study investigated the performance of a desiccant coated microchannel heat exchanger (DMHE) and fin-tube heat exchanger (DFHE). The study mainly focused on geometrical parameters such as fin pitch and thickness, flat tube pitch and thickness, and desiccant thickness. ▪ The results show that DMHE outperforms DFHE in terms of thermal coefficient of performance, and air velocity was identified as the most influential parameter for performance. ▪ The experiment was limited to DMHE only and model validation was limited to comparing heat and moisture transfer coefficients. The model was not validated for dehumidification capacity and outlet air temperature with experimental results. ▪ The study did not discuss the transient evaluation of local air and bed temperature. Air temperature at the outlet was reported. ▪ The study used hot water for bed regeneration only. Effect of internal cooling during adsorption was not investigated.
[48]	Experiment (2023)	Encapsulated composite desiccant (AFLi30@P), Type A silica gel	▪ The study reports synthesis of a new encapsulated composite desiccant (AFLi30@P) membrane with high water uptake capacity 3.8g/g. Only adsorption isotherm was reported, and desorption isotherm was overlooked. ▪ Although new desiccant was membrane, it's performance was compared with Type A silica gel instead of comparing other membranes.

			▪ Temperature distribution of DCHE was reported at different time steps for regeneration process only. Only qualitative data obtained potentially by an infrared camera were provided, and no quantitative data was reported. Besides, the authors did not provide details of the temperature measurement device and process. ▪ Only the influence of chilled water temperature on moisture uptake difference was investigated, effect of chilled water flowrate was overlooked. ▪ The authors compared the performance of their DCHE with new composite membrane against DCHEs from literature (coated with different desiccants) and showed their DCHE can outperform the other DCHEs. But the inlet conditions for DCHE with AFLi30@P were different than the studies they compared with.
[33]	Experiment (2019)	Silica gel (SCHE), Silica gel with Sodium Acetate (SASCHE), Silica gel with Potassium Formate (PSCHE)	▪ SASCHE exhibited 10% and 30% higher dehumidification capacity as compared to PSCHE and SCHE, respectively. ▪ Despite new composite desiccants being synthesized, their adsorption/desorption isotherm and stability under cyclic operation were not reported. ▪ Only the chilled water temperature variations were investigated and chilled water flow rate variations was overlooked. ▪ Key performance indicators were outlet air temperature, outlet air humidity ratio, heating capacity and heat recovery efficiency. Thus, the article overlooks the transient evaluation of local air and bed temperatures. ▪ Cycle duration was fixed to 720 sec. Thus, the article does not discuss how internal cooling can influence the performance for different cycle durations.
[40]	Experiment (2024)	Silica gel with LiCl (5w%)	▪ The study investigated the performance of a silica gel and LiCl coated DCHE for normal and deep dehumidification (i.e., air dew point temperature below 0 ℃). ▪ Key performance indicators were moisture removal capacity (MRC) (g/kg), COP defined as the ratio of enthalpy change of air during dehumidification to the heat exchange with water during both dehumidification and regeneration. ▪ The study did not report the adsorption/desorption isotherm of the synthesized composite desiccant. Also, the article did not report dehumidification capacity which is a key performance indicator commonly used in the literature. ▪ The article did not investigate the air temperature change locally as well as at the outlet and local bed temperature change due to the internal cooling. ▪ Despite water inlet and outlet temperatures were used in COP estimation, but these data were not reported in the article.
[49]	Experiment and modeling (2024)	Composite MIL-100 (Fe) and silica gel	▪ A DCHE was prepared using composite MIL-100 (Fe) and silica gel and its performance was evaluated for three different binder types (PVP, PVA and PVB). ▪ The results showed that MRC of composite MOF could be as high as 149.63% compared to silica gel coating and the cost of composite MOF was 78.04% lower compared to pure MOF. ▪ Although the article reported synthesis of new composite desiccant, the performance of DCHE was evaluated using a numerical model. Validation of the model was conducted using data from the literature. ▪ Model parametric study was mainly conducted for structural parameters (fin height, spacing and coating thickness). For

			operating conditions only chilled water temperature and initial moisture content of the bed were considered. ▪ Thus, the article did not discuss the influence of inlet air humidity, air flow rate, water flow rate, cycle duration. Also, the article did not report on the local distribution of air and bed temperatures.
[50]	Experiment (2024)	MIL-101(Cr)	▪ MIL-101(Cr) was synthesized using hydrothermal method and its equilibrium water uptake capacity was reported as 1.17g/g at 90% RH. The adsorption isotherm exhibited a stepwise uptake at 35% to 45% RH range. However, the authors did not report the desorption isotherm of the synthesized MOF. ▪ Performance of MOF coated DCHE was evaluated experimentally under a wide range of conditions and using two different layouts of DCHE (series and parallel). The reported dehumidification capacities were in the range of 0.26-0.43 kg/h and 0.24-0.40 kg/h for the parallel and series modes respectively. ▪ The study only reported the dehumidification performance of the DCHE and overlooked the air and water temperature at the outlet as well as temporal evaluation of local air and bed temperatures.
[51]	Experiment (2025)	Composite desiccant (Silica gel, $CaCl_2$ 12 wt%, HEC 3.3 wt%)	▪ A counter flow DCHE featuring internal embodiment and coated with composite desiccant were tested experimentally under variety of operating conditions. ▪ Key performance indicators were dehumidification capacity, cooling capacity, $COP_{thermal}$, specific humidity effectiveness and relative humidity effectiveness to be reported in the range 6.4-12.8 g/kg_{DA}, 454-1545 W, 0.18-0.56, 54%-73% and 69%-85%, respectively. ▪ The article reported only adsorption isotherm of composite desiccant but did not report the desorption isotherm. Also, the article strongly claims composite desiccant used in the experiment can be regenerated at ultra-low temperature (i.e., 50 ℃), but according to other literature, at 50 ℃ silica gel-based composites cannot be fully regenerated. ▪ The article compared the performance with other DCHE from the literature, but the authors did not mention what desiccants were used in that literature, which makes the performance comparisons vague. ▪ The article reported 90% energy savings compared to conventional vapor compression refrigerant systems but did not provide the details and basis of this estimation. ▪ The articles reported air temperature at the outlet for the base case only but did not show how it affected under different operating conditions. Also, the article overlooked local distribution of air and bed temperatures.
[52]	Modeling (2024)	Silica gel	▪ The study compared the performance of a wavy fin DCHE with a plain fin DCHE and the results showed that wavy fin configuration could achieve 61% higher dehumidification capacity. ▪ The article did not provide any information on the desiccant used including its adsorption/desorption isotherm. ▪ The model assumed binder quantity is small and has no effect in the modelling which is not practical. ▪ The article reported only the air temperature at the outlet and overlooked the local air and bed temperature distribution.

Although DCHEs show great potential for efficient dehumidification, their current manufacturing typically relies on coating desiccant materials onto heat exchange substrates using polymer binders. Several studies have highlighted that the use of binders can significantly reduce the dehumidification capacity due to pore blockage effects [53, 54]. To assess the true dehumidification potential of desiccant materials, employing them in a binder-free configuration is essential. To address this challenge, in our previous studies [55, 56], we reported the performance of a multilayer fixed-bed binder-free desiccant dehumidifier (MFBDD) device, as illustrated in **Figure 1**. The device utilized a silica-based high-purity spherical Micro Sphere Gel (M.S. Gel) as the desiccant (**Figure 1e** represents the scanning electron microscope (SEM) image of spherical M.S. Gel particles), manufactured by AGC, Inc., Japan, which exhibits an S-shaped (Type IV) adsorption–desorption isotherm. The adsorption and regeneration performance of the MFBDD device was systematically evaluated through both experimental investigations [55, 57] and numerical modeling studies [56, 58].

Due to its sheet-type configuration (**Figure 1b**) arranged in a multilayer assembly (**Figure 1a**), the MFBDD device demonstrated minimal flow restriction, achieving nearly 98% lower pressure drop compared to conventional rotary desiccant wheels [55]. Besides, the MFBDD device employed a binder-free configuration, wherein stainless steel (SS) mesh (**Figure 1c and 1d** represent the photograph and SEM image of SS mesh, respectively) was used as the structural support to house the M.S. Gel desiccant instead of coating them using polymer binder. This approach effectively eliminated the pore blockage issue and facilitated higher water vapor uptake by the pure M.S. Gel desiccant. As a result, the MFBDD device achieved approximately 36% improvement in moisture removal capacity compared to a typical rotary desiccant wheel [55]. **Figure 1f** shows the optical microscope image of M.S. Gel desiccants loaded within the SS mesh.

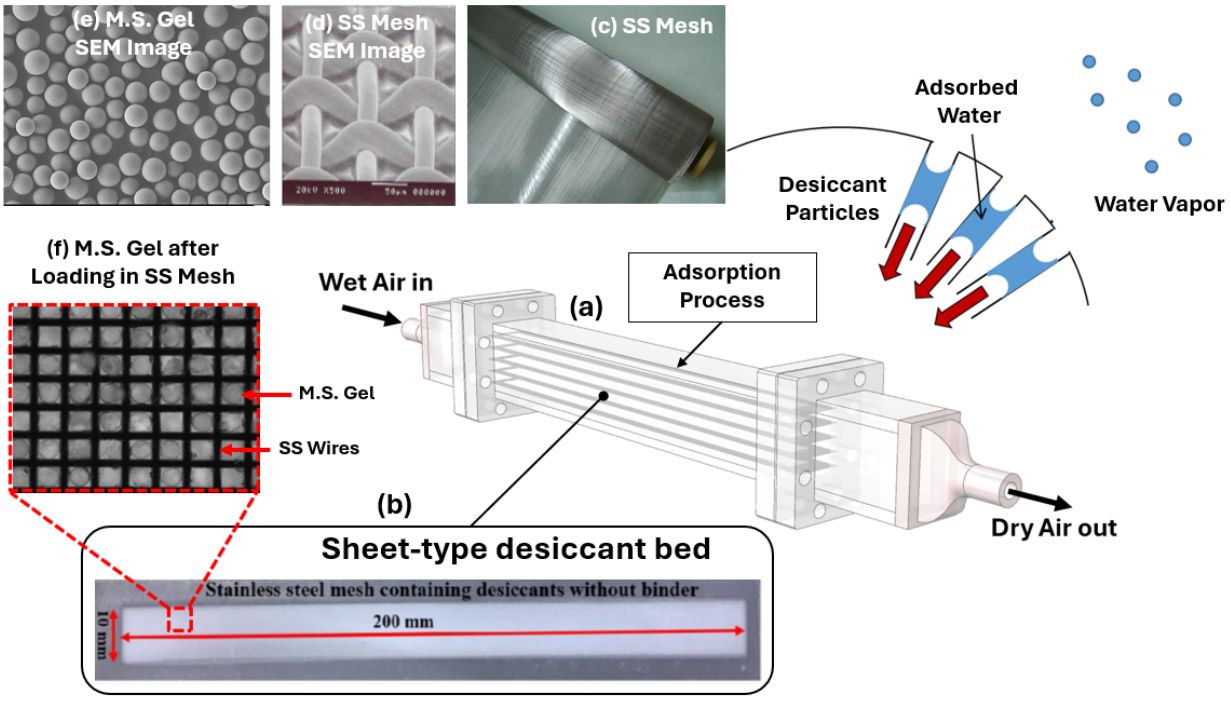

Figure 1. Illustration of multilayer fixed-bed binder-free desiccant dehumidifier (MFBDD) proposed by Shamim et al. [55]. (a) MFBDD device showing the arrangement of desiccant sheets with inlet and

outlet airflow directions, and water vapor adsorption mechanism in desiccant particles; (b) photograph of sheet-type desiccant bed filled with M.S. Gel; (c) photograph of SS mesh used to fabricate desiccant bed [59]; (d) SEM image of SS mesh showing the voids between SS wires [59]; (e) SEM image of M.S. Gel showing the spherical particles [60] and (f) Optical microscope image of the portion of desiccant bed filled with M.S. Gel.

While the MFBDD demonstrated promising dehumidification performance, its potential for further performance enhancement by integrating internal cooling remains unexplored. Lily et al. [61] conducted an optimization study of a water-cooled MFBDD device using a lumped parameter model. However, the effects of internal cooling and step-shape isotherms on the coupled mass and heat transfer characteristics, along with the underlying physics, were not discussed in sufficient detail. In this study, we therefore investigate the heat and mass transfer performance of the MFBDD in greater depth by incorporating internal cooling and employing a MOF-based composite desiccant (MIL-101/GO-6, where GO-6 represents 6 wt.% of Graphite Oxide) using a physics-based one-dimensional (1D) model framework. The composite MOF considered in this study was reported by Yan et al. [62], and exhibited very high water uptake capacity (close to 1.6 g/g) within a narrow relative humidity range (35% - 47%). To the best of authors' knowledge and based on the review of literature presented earlier in **Table 1**, the dehumidification performance of such a composite desiccant characterized by high water vapor uptake within a narrow relative humidity range has not yet been reported for an internally cooled binder-free dehumidifier configuration.

Furthermore, the existing literature largely overlooks the transient evaluation of local bed and air temperature profiles, as well as the influence of internal cooling on dehumidification performance across different cycle durations. These parameters are critical for advancing the fundamental understanding of the adsorption process within the desiccant bed and for identifying pathways to enhance system performance. Accordingly, the present study provides a detailed analysis of these parameters and their impact on overall dehumidification behavior. Finally, the present study reports a detailed parametric study elucidating how internal cooling influences the relative humidity within the bed, and how simultaneous enhancement of the convective heat transfer coefficient and the heat exchange surface area between the chilled water and desiccant bed facilitates near-isothermal dehumidification by maintaining the bed's relative humidity within the target narrow range corresponding to the step location in the desiccant's isotherm. Such discussions, which deepen the fundamental understanding of adsorption mechanisms in internally cooled desiccant systems, also remain scarce in the literature.

To be noted that 1D model is often preferred over computational fluid dynamics (CFD) or lumped parameter models as CFD requires intensive computation, and the lumped model cannot provide information on the local distribution of parameters — such as humidity (mass transfer) and temperature (heat transfer) — due to the assumption of spatial uniformity. In contrast, 1D models simplify the governing equations along a single spatial direction, significantly reducing computational time while retaining most of the key physics-based phenomena [63]. Due to their inherently modular and computationally lightweight nature, 1D models are easier to scale up and integrate into system-level simulations, making them ideal for training machine-learning algorithms requiring large datasets. Hence, in this study, a 1D model was developed based on the coupled mass and energy conservation equations to establish a framework for future performance optimization of MFBDD using data-driven and AI-assisted methodologies.

The developed model was validated for both adsorption and regeneration processes using experimental data [55, 57] and CFD results [56, 58] from previous studies conducted on the MFBDD device

without water circulation. Upon validation, the model was extended to evaluate adsorption performance in the MFBDD device integrated with chilled water cooling. For the water-cooled cases, MIL-101/GO-6 was selected as the desiccant due its high water uptake capacity within a narrow relative humidity range [62]. The effects of varying chilled water flow velocities and inlet temperatures were investigated, and a comprehensive parametric study was conducted to identify the key factors enabling isothermal dehumidification under water-cooled operation. The proposed 1D model provides a framework for system-level performance evaluation that accounts for separate sensible and latent cooling processes, facilitating the scale-up of the MFBDD device and its integration within building HVAC systems for improved energy management.

2 Dehumidifier Design and Materials

2.1 Original MFBDD Design

Figure 2 illustrates the geometry and dimensions of the MFBDD desiccant sheet used for heat and mass transfer analysis in the current 1D model. As shown in **Figure 2a**, the central region, measuring 200 mm in length and 10 mm in width, contains the M.S. Gel desiccants loaded between SS mesh layers. The frame dimensions are 210 mm × 20 mm. The cross-sectional view (**Figure 2b**) shows a vertical stack of five desiccant sheets, each 1 mm thick, separated by air channels. This configuration results in a total height of 30 mm and a width of 10 mm (excluding the SS frame). The calculated cross-sectional area for five desiccant sheets is 50 mm², while the cross-sectional area for air channels is 250 mm². This design offers a balanced trade-off between desiccant loading and airflow passage, promoting efficient adsorption with minimal pressure drop.

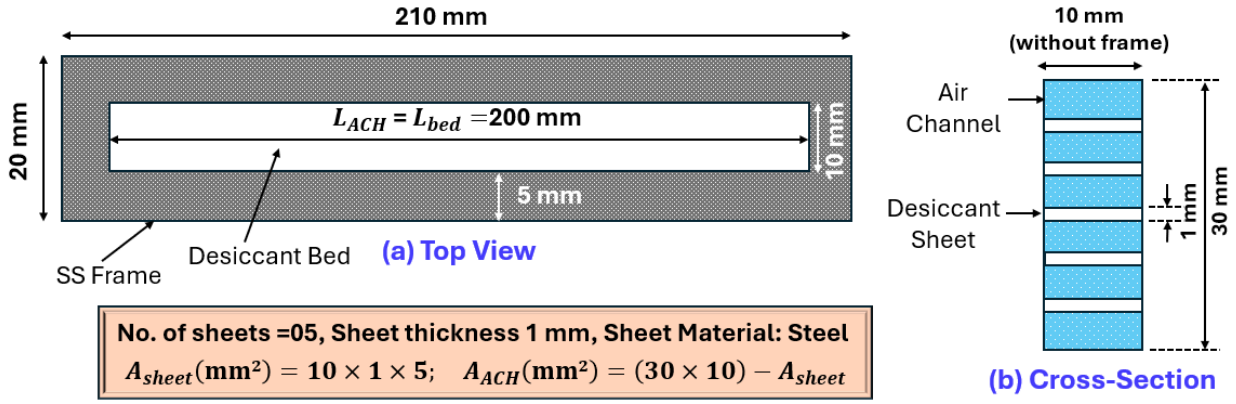

Figure 2. Physical dimensions of the desiccant sheet and air-channels in MFBDD prototype device. (a) top view of the desiccant sheet; (b) cross-section view of the MFBDD device showing air channels (blue area) and five desiccant sheets (white stripes). Total five desiccant sheets were used in MFBDD prototype. A_{sheet} represents total cross-section area for five desiccant sheets and A_{ACH} represents total cross-section area for six air channels. The length of air channel (L_{ACH}) and desiccant bed are assumed to be equal.

2.2 MFBDD with Internal Cooling

Figure 3 depicts the structure of the modified MFBDD desiccant sheet, incorporating hollow water channels embedded within the 5 mm-wide stainless steel (SS) frame. This configuration enables concurrent airflow over the desiccant layer and water flow along both lateral edges of the sheet. During the adsorption cycle, the exothermic heat generated by water vapor uptake is effectively removed through heat exchange

with the circulating cooling water. This thermal management suppresses temperature rise within the desiccant bed, thereby enhancing adsorption capacity and mass transfer rates. The device can support both co-current and counter-current flow of air and water (this study uses a co-current flow), offering flexibility to maximize heat and mass transfer performance. The length of the water channel (L_{WCH}) is assumed to be the same as the length of the air channel (L_{ACH}) (i.e., 200 mm).

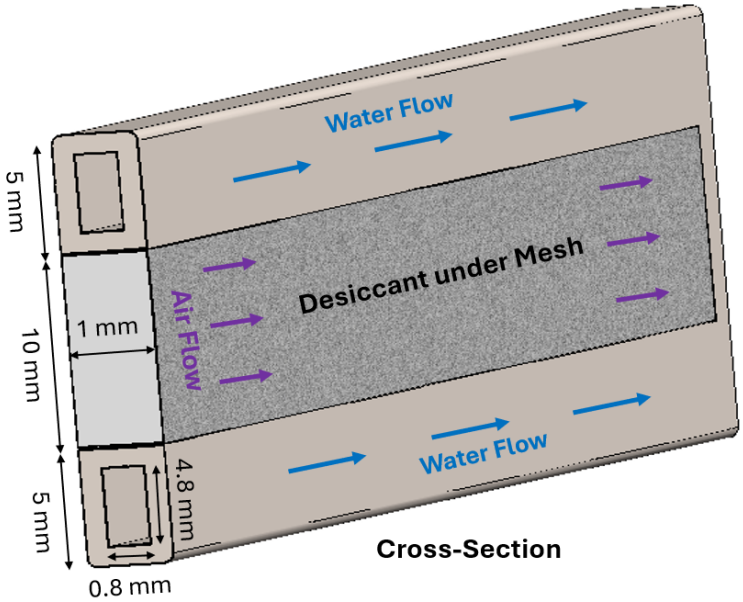

Figure 3. Three-dimensional view of the modified MFBDD device including water channels. Water channels can be made on two sides by using hollow SS frames.

2.3 Desiccant Materials

The M.S. Gel desiccant (99.9% SiO_2) employed in the MFBDD device was characterized by a pore diameter of 2.7 nm, pore volume 0.60 ml/g, particle diameter 63–210 (63 mm down ≤ 8.0% and 210 mm up ≥ 10.0%), and BET surface area 897 m^2/g [55]. The adsorption and desorption isotherms of M.S. Gel was measured at 298.15 K as presented in **Figures 4a and 4b**, respectively (solid red lines). The corresponding fitted curves using the Langmuir–Sips equation [64] are shown as dashed red lines in the above figures. **Figure 4c** shows the adsorption and desorption isotherms of MIL-101/GO-6 at 298.15 K, which exhibits a BET surface area of 3522 m^2/g and a total pore volume of 1.78 cm^3/g, as reported by Yan et al. [62]. MIL-101/GO-6 was employed in the water-cooled MFBDD owing to its step-shaped adsorption isotherm within a narrow relative humidity range, enabling a performance comparison with M.S. Gel, which exhibits an S-shaped isotherm. Due to the absence of a single isotherm model capable of accurately capturing the step-shape behavior of MIL-101/GO-6, piecewise-linear equations were employed to fit the isotherm across three distinct relative humidity ranges: 0–35%, 35–47%, and 47–100%, as shown in **Figures S1a-c,** respectively, in the SI. The thermophysical properties and total mass of M.S. Gel and MIL-101/GO-6 desiccants utilized in the present study are provided in **Table 2** and **Table 3**, respectively.

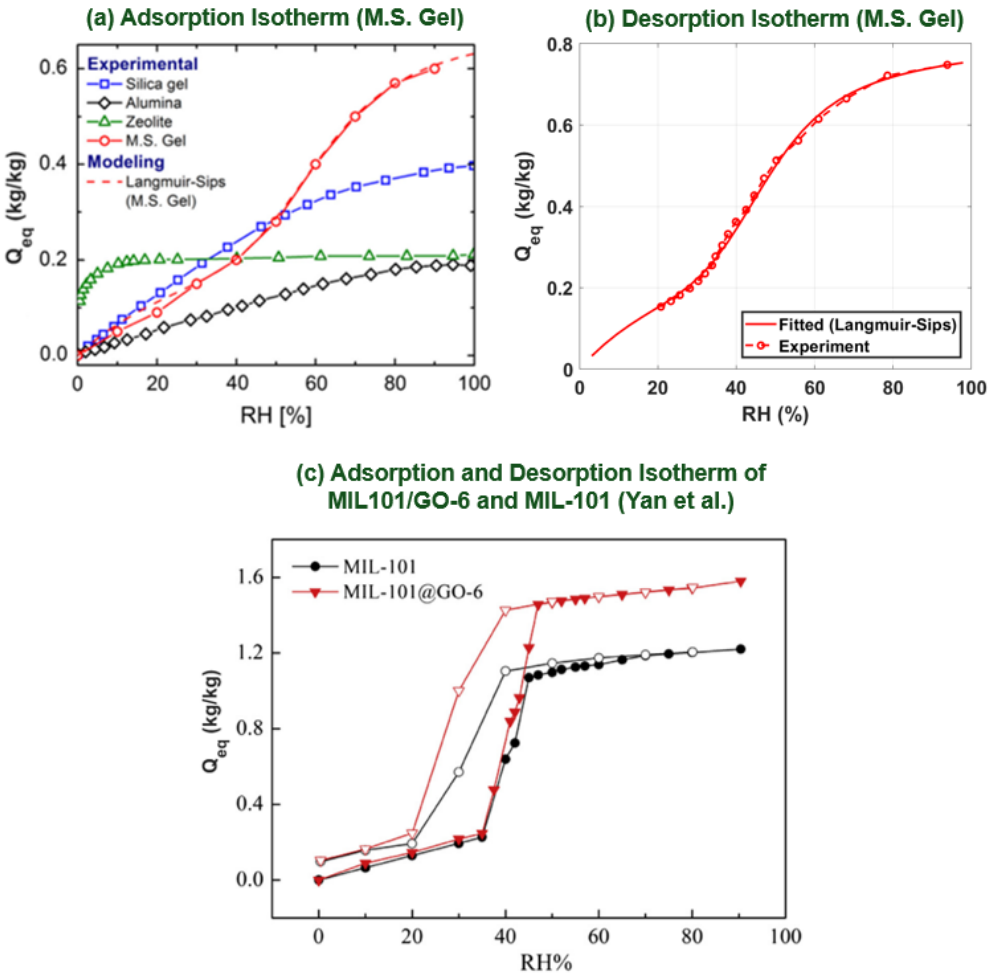

Figure 4. Adsorption and desorption isotherms of the desiccants considered in the present study. (a) adsorption isotherm (experimental and fitted) of M.S. Gel [56]; (b) desorption isotherm (experimental and fitted) of M.S. Gel; (c) adsorption/desorption isotherms of MIL-101/GO-6 and MIL-101 reported in [62].

Table 2. Thermo-physical properties of M.S. Gel

Properties		Value	Unit	Ref.
Density		1100	kg/m^3	[56]
Specific heat capacity		921	J/kg. K	
Enthalpy of Adsorption		2.26×10^6	J/kg	
Adsorption rate constant		3.5×10^{-3}	s^{-1}	
[1]Bed porosity (ε_{bed})	Adsorption	0.3	-	[56, 61]
	Regeneration	0.5	-	[58]
[2]Mass of desiccant in five sheets	Adsorption	0.0076	kg	[55]
	Regeneration	0.0055	kg	
Thermal conductivity		0.34	W/m.K	[65]

[1]Bed porosity for adsorption and regeneration cases with M.S. Gel desiccant were adopted from our previous modeling studies [56, 58, 61]. In previous studies this parameter was considered as a fitting parameter to obtain a good agreement between numerical and experimental results.

[2]The mass of M.S. Gel was measured experimentally during the fabrication of desiccant sheets.

[3]Table 3. Thermo-physical properties of MIL-101/GO-6

Properties	Value	Unit	Ref.
Density	1305	kg/m^3	[66]
Specific heat capacity	1200	J/kg. K	
Enthalpy of Adsorption	2.52×10^6	J/kg	
[4]Adsorption rate constant	3.5×10^{-3}	s^{-1}	Assume same as M.S. Gel
[5]Bed porosity	0.42	-	-
Mass of desiccant in five sheets	0.0076	kg	-
[6]Thermal conductivity	0.126	W/m.K	[67]

Notes

[3]Due to the limited availability of thermophysical data for MIL-101/GO-6 in the literature, the properties of MIL-101/GO-5, as reported by Xia and Li [66], have been adopted in this study. Additionally, the bed porosity for MIL-101/GO-6 has been adjusted to ensure an equivalent desiccant mass between MIL-101/GO-6 and M.S. Gel, allowing for a meaningful performance comparison.

[4]No reported values for the adsorption rate constant of MIL-101(Cr)/GO are currently available in the literature. However, Wee et al. [68] report that the adsorption rate constant for MIL-101(Cr), across various binder ratios, is on the order of 10^{-4} s^{-1}. Given that MIL-101(Cr)/GO exhibits a higher adsorption capacity than its parent material, MIL-101(Cr), the same adsorption rate constant as that of M.S. Gel is assumed in this study for the sake of modeling simplicity.

[5]Bed porosity for MIL-101/GO-6 was estimated assuming equal mass of M.S. Gel (i.e., 0.0076 kg in 5 sheets). The volume of each 1.0 mm thick sheet is 2×10^{-6} m^3as per dimensions shown in Figure 2. Bed porosity can be estimated according to the expression: $\varepsilon_{bed} = 1 - {V_s}/{(V_s + V_{sheet})}$, where V_s and V_{sheet}represents volume of solid and sheet, respectively.

[6]Due to the lack of available data for MIL-101/GO in the literature, the thermal conductivity of MIL-101(Cr)-5%GrO at 303 K, as reported by Elsayed et al. [67], has been adopted in the present study.

3 Model Description and Simulation Method

3.1 Model Assumptions

- Equations of mass and energy balance are solved in axial direction (X-axis) only.
- The bed porosity is assumed to be uniform in axial direction.
- Temperature dependency of desorption isotherms is not considered in the modeling of regeneration process.
- Only the macroscopic properties (i.e., inter-particle porosity and adsorption/desorption rate constant of desiccant bed) are considered in the governing equations to model moisture transport in the desiccant bed.

- The influence of intra-particle porosity (i.e., transport inside the particle) is assumed to be included in the experimentally measured adsorption/desorption isotherms.
- The convective heat transfer coefficients between the desiccant bed and flowing air, and between desiccant and ambient, as well as adsorption/desorption rate constants of the desiccant bed are taken as fitting parameters for simplicity and due to the lack of appropriate models.
- Saturation vapor pressure and partial vapor pressure of water vapor in the desiccant bed is estimated using average desiccant temperature assuming local thermal equilibrium between the desiccant and air within the bed.
- Thermal resistance between the desiccant bed and water channel is neglected due to the tiny thickness (0.1 mm) of the channel wall thickness.

3.2 Governing Equations: Mass and Energy Banalce

Mass balance: The coupled heat and mass transfer processes in the MFBDD desiccant bed are described by a series of 1D partial differential equations. The mass balance (Eq. (1)) accounts for the transient accumulation of moisture content in the desiccant bed, convective and diffusive transport of water vapor in air, and the adsorption rate within the desiccant matrix.

$$\frac{dW}{dt} + u_{air}\frac{dW}{dx} = D_{air}\frac{d^2W}{dx^2} - \frac{\rho_{des}\,(1-\varepsilon_{bed})\,A_{Sheet}}{\rho_{air}\,(A_{ACH}+\varepsilon_{bed}A_{Sheet})}\frac{dQ_{bed}}{dt} \qquad \text{Eq. (1)}$$

In above equation, A_{Sheet} = 5×10^{-5} m^2, A_{ACH} = 2.5×10^{-4} m^2, D_{air} is taken as 2.82 × 10^{-5} $m^2\ s^{-1}$; and the values of inter-particle porosity in the bed, $\boldsymbol{\varepsilon_{bed}}$ used for different cases are listed in **Table 1** and **Table 2.** Modeling of the source term $\frac{dQ_{bed}}{dt}$ representing the rate of moisture adsorption will be discussed in **section 3.3.**

Energy balance in the air channel: The energy balance in the air channel (Eq. (2)) considers unsteady and convective heat transfer, axial conduction, and heat exchange with the desiccant bed through the interface area.

$$\frac{dT_{air}}{dt} + u_{air}\frac{dT_{air}}{dx} = \alpha_{air}\frac{d^2T_{air}}{dx^2} + \frac{h_{sa}\ A_{sa}}{(A_{ACH}+\varepsilon_{bed}A_{Sheet})\,\rho_{air}\,C_{p,air}\,L_{ACH}}(T_{bed}-T_{air}) \qquad \text{Eq. (2)}$$

In Eq. (2), $A_{sa} = 2\times10^{-2}\ m^2$, α_{air} =1.9 × 10^{-5} $m^2\ s^{-1}$, $\rho_{air} = 1.225\ kg\ m^{-3}$, and $C_{p,air} = 1.027\times10^3\ J\ kg^{-1}\ K^{-1}$. h_{sa} is treated as a fitting parameter and is taken as 7.9 $Wm^{-2}.K^{-1}$ for adsorption and 25 $Wm^{-2}.K^{-1}$ for regeneration in the present study [56, 58, 61].

Energy balance in the water channel: The energy balance in the water channel (Eq. (3)) accounts for thermal transport and heat transfer from the desiccant bed to the circulating water. Due to the minimal channel thickness (0.1 mm), the heat capacity and conduction resistance of the water channel is neglected.

$$\frac{dT_w}{dt} + u_w\frac{dT_w}{dx} = \alpha_w\frac{d^2T_w}{dx^2} + \frac{h_{sw}\ A_{sw}}{A_{WCH}\,\rho_w\,C_{p,w}\,L_{WCH}}(T_{bed}-T_w) \qquad \text{Eq. (3)}$$

In the above equation, constants A_{WCH} = 3.84 × 10^{-6} m^2, A_{sw}= 3.2 × 10^{-4} m^2, $L_{WCH} = 0.2\ m$, α_w= 1.41 × 10^{-7} $m^2\ s^{-1}$ and $C_{p,w}$ = 4185 $Jkg^{-1}K^{-1}$ (evaluated at 288.15 K). ρ_w is modeled as functions of temperature by fitting a third-order polynomial equation to the experimental data of water density across a range of temperatures sourced from reference [69], as shown in **Figures S2** in the SI. Modeling of the term h_{sw} will be discussed in **section 3.4.**

Energy balance in the desiccant bed: The energy balance within the desiccant bed is modeled under two scenarios. For the dry case (Eq. (4)), heat accumulation is governed by conduction, adsorption heat release, convective exchange with air, and ambient heat loss. For the water-cooled case (Eq. (5)), an additional term is included to represent convective heat transfer between the desiccant bed and the cooling water. In both cases, the heat of adsorption is modeled as a source term dependent on the adsorption rate.

$$\frac{dT_{bed}}{dt} = \alpha_{bed}\frac{d^2T_{bed}}{dx^2} + \frac{H_{ads}m_{des}}{m_{bed}C_{p,bed}}\frac{dQ_{bed}}{dt} - \frac{h_{sa}\ A_{sa}}{m_{bed}C_{p,bed}}(T_{bed} - T_{air}) - \frac{h_{amb}}{m_{bed}C_{p,bed}}(T_{bed} - T_{amb}) \quad \text{Eq. (4)}$$

$$\frac{dT_{bed}}{dt} = \alpha_{bed}\frac{d^2T_{bed}}{dx^2} + \frac{H_{ads}m_{des}}{m_{bed}C_{p,bed}}\frac{dQ_{bed}}{dt} - \frac{h_{sa}\ A_{sa}}{m_{bed}C_{p,bed}}(T_{bed} - T_{air}) - \frac{h_{sw}\ A_{sw}}{m_{bed}C_{p,bed}}(T_{bed} - T_w) - \frac{h_{amb}}{m_{bed}C_{p,bed}}(T_{bed} - T_{amb}) \quad \text{Eq. (5)}$$

In Eq. (4) and Eq. (5), H_{ads} is taken as $2.26 \times 10^6\ J\ kg^{-1}$ for M.S. Gel [56], and $2.52 \times 10^6\ J\ kg^{-1}$ for MIL-101/GO-6 [66]. Here, h_{amb} is used as a fitting parameter and its values are adopted as $0.104\ W\ K^{-1}$ for adsorption and $0.25\ W\ K^{-1}$ for regeneration, for the total heat exchange surface area of the dehumidifier with the ambient [56].

Boundary and initial conditions: The boundary conditions used to solve the equations (Eq. (1) through Eq. (5)) are listed in **Table S1**. The initial conditions used in the model validation for adsorption [56] and regeneration [58] are listed in **Table S2** and **Table S3**, respectively, in the SI.

3.3 Modeling of Adsorption Kinetics

The adsorption kinetics within the desiccant bed are modeled using the Linear Driving Force (LDF) approach [70] as expressed in Eq. (6), which assumes that the rate of adsorption is proportional to the difference between the equilibrium adsorption capacity Q_{eq} and the instantaneous adsorption value Q.

$$\frac{dQ_{bed}}{dt} = K_{LDF}(Q_{eq} - Q_{bed}) \quad \text{Eq. (6)}$$

In Eq. (6), K_{LDF} is a fitting parameter and adopted as $3.5 \times 10^{-3}\ s^{-1}$ for both adsorption and regeneration cases with M.S. Gel and MIL-101/GO-6 based on our previous studies [56, 61]. To initialize the numerical iteration for Eq. (6), the initial mass of water in the desiccant bed is taken as $6 \times 10^{-5}\ kg\ kg^{-1}_{M.S.\ Gel}$ (representing initial mass of water close to zero) and $4 \times 10^{-1}\ kg\ kg^{-1}_{M.S.\ Gel}$ (representing 2.3×10^{-3} kg water in 5.5×10^{-3} kg M.S. Gel) for adsorption and regeneration, respectively as estimated in our previous modeling studies [58, 61].

The equilibrium uptake Q_{eq} of M.S. Gel is modeled using the Langmuir–Sips isotherm model which captures both Type I (Langmuir) and Type V (Sips) adsorption behavior through a two-term expression as expressed in Eq. (7) [64]:

$$Q_{eq} = a\left(\frac{b_1\varphi}{1 + b_1\varphi} + \frac{b_2\varphi^n}{1 + b_2\varphi^n}\right) \quad \text{Eq. (7)}$$

here, parameters a, b_1, b_2 and n are fitting parameters to fit the experimental adsorption and desorption isotherms of M.S. Gel. **Table S4** lists the numerical values of the parameters a, b_1, b_2 and n.

In Eq. (7), φ is the relative humidity of air within the bed and is defined as the ratio of the partial vapor pressure P_v to the saturation vapor pressure P_{sat} as below [56]:

$$\varphi = \frac{P_v}{P_{sat}} \times 100 \quad \text{Eq. (8)}$$

The saturation vapor pressure and partial vapor pressure are determined using Eq. (9) and Eq. (10), respectively [56]:

$$P_{sat} = 610.78\ exp\left(\frac{17.27(T_{bed,avg} - 273.15)}{(T_{bed,avg} - 35.85)}\right) \quad \text{Eq. (9)}$$

$$P_v = \frac{W_{avg}\ \rho_{air}\ R\ T_{bed,avg}}{M_w} \quad \text{Eq. (10)}$$

Here, constants $R = 8.3145\ Jmol^{-1}K^{-1}$, $M_w = 18.015 \times 10^{-3}\ kg\ mol^{-1}$. In the equations of P_{sat} and P_v, the average temperature of the bed ($T_{bed,avg}$ in K) is used assuming a local thermal equilibrium between the desiccant and air within the bed [56]. In Eq. (10), $W_{avg}$is the average air specific humidity within the air channel.

3.4 Modeling Convective Heat Transfer Coefficient of Water

The convective heat transfer coefficient between the cooling water and the desiccant bed, h_{sw}, is calculated using the Nusselt number correlation as expressed in Eq. (11) [61]. The Nusselt number is estimated from the empirical correlation provided in Eq. (12), which is valid for laminar, fully developed flow. The Reynolds number and Prandtl number are estimated using Eq. (13) and Eq. (14), respectively, for different water temperatures and flow conditions. The hydrodynamic entry length for laminar flow is calculated using Eq. (15) and is found to be 104.19 mm at a water flow velocity of 1 $m\ s^{-1}$. Since this entry length is significantly smaller than the total length of the water channel, the flow within the channel is assumed to be fully developed.

$$h_{sw} = \frac{Nu\ k_w}{D_h}\gamma, where\ \gamma = {}^{1}/_{6} \quad \text{Eq. (11)}$$

$$Nu = 0.00881\ Re^{0.8991}Pr^{0.391} \quad \text{Eq. (12)}$$

$$Re = \frac{\rho_w\ D_h\ u_w}{\mu_w} \quad \text{Eq. (13)}$$

$$Pr = \frac{C_{p,w}\ \mu_w}{k_w} \quad \text{Eq. (14)}$$

$$L_{entry} = 0.05\ D_h\ Re \quad \text{Eq. (15)}$$

Here, $k_w = 0.59\ Wm^{-1}K^{-1}$, treated as constant at 288.15 K. μ_w is modeled as functions of temperature by fitting a third-order polynomial equation to experimental data of water dynamic viscosity across a range of temperatures sourced from reference [71], as shown in **Figure S3** in the SI.

3.5 Auxiliary Equations

Several other auxiliary equations are used to solve the governing equations of mass and energy as listed in Eq. (16) through Eq. (23) [56, 61]. In Eq. (16), the total mass of the desiccant bed, m_{bed}, is the sum of the mass of the desiccant material (m_{des}) and the mass of air within the bed ($m_{air\_in\_bed}$). The thermophysical properties of desiccants (e.g., density (ρ_{des}), specific heat capacity ($C_{p,des}$) and thermal conductivity (k_{des})) for M.S. Gel and MIL-101/GO-6 used in Eq. (16) through Eq. (23) are listed earlier in **Table 1 and Table2**, respectively.

$$m_{bed} = m_{des} + m_{air\_in\_bed} \quad \text{Eq. (16)}$$

$$m_{des} = (1 - \varepsilon)\, \rho_{des}\, A_{sheet}\, L_{ACH} \quad \text{Eq. (17)}$$

$$m_{air\_in\_bed} = \varepsilon_{bed}\, \rho_{air}\, A_{ACH}\, L_{ACH} \quad \text{Eq. (18)}$$

$$C_{p,\,bed} = \varepsilon_{bed}\, C_{p,air} + (1 - \varepsilon_{bed}) C_{p,des} \quad \text{Eq. (19)}$$

$$\alpha_{bed} = \frac{k_{bed}}{(\rho C_p)_{bed}} \quad \text{Eq. (20)}$$

$$k_{bed} = \varepsilon_{bed}\, k_{air} + (1 - \varepsilon_{bed}) k_{des} \quad \text{Eq. (21)}$$

$$(\rho C_p)_{bed} = \varepsilon_{bed}\, \rho_{air}\, C_{p,air} + (1 - \varepsilon_{bed})\, \rho_{des}\, C_{p,des} \quad \text{Eq. (22)}$$

$$k_{air} = \alpha_{air}\, \rho_{air}\, C_{p,air} \quad \text{Eq. (23)}$$

3.6 Simulation Method and Performance Indicators

The conservation equations of mass and energy, along with the supporting equations described in the previous sections, are solved in MATLAB (version R2024b) using the method of lines approach [72]. The system of partial differential equations (Eqs. (1)–(5)) is transformed into a set of ordinary differential equations (ODEs) by discretizing the spatial derivatives: first-order derivatives are approximated using the backward-difference scheme, while second-order derivatives are treated with the central-difference scheme. The resulting ODE system, along with the associated algebraic equations, is solved using MATLAB's ode23s solver. The air channel, desiccant bed, and water channel are each discretized into 50 uniform segments (N=50, where N represents the total number of segments, and N_1, N_2, N_3….N_{50} representing individual segment numbers), corresponding to a spatial resolution of 0.4 m per segment. For all cases, inlet, middle, and outlet are defined at the 2nd (N_2), 25th (N_{25}), and 49th (N_{49}) segment. The 1st and 50th segments are used to supply inlet and outlet boundary conditions, respectively. A fixed time step of 1 second is used, and simulations are conducted over a total period of 900 seconds.

The performance of the MFBDD device is evaluated based on four key indicators: (i) total mass of water vapor adsorbed in or desorbed from the bed (g), (ii) dehumidification or regeneration capacity ($g\ kg_{DA}^{-1}$), (iii) air temperature difference between outlet and inlet of the dehumidifier (ΔT_{air}) in K, and (iv) the mean bed temperature (K). The definition of these performance indicators is available in our previous studies with the MFBDD device [55-58, 61]. The numerical expressions used in the present study to estimate these performance indicators at each individual time-step are expressed through Eqs. (24)–(28).

$$\text{Total mass adsorbed or desorbed (g)} = Q_{bed} \times m_{des} \times 1000 \quad \text{Eq. (24)}$$

$$\text{Dehumidification capacity } (DC)\ (g\ kg_{DA}^{-1}) = (W_{in} - W_{out}) \times 1000 \quad \text{Eq. (25)}$$

$$\text{Regeneration capacity } (g\ kg_{DA}^{-1}) = (W_{out} - W_{in}) \times 1000 \quad \text{Eq. (26)}$$

$$\Delta T_{air}\ (K) = T_{air\_out} - T_{air\_in} \quad \text{Eq. (27)}$$

$$\text{Mean bed temperature } (K) = Mean\left(T_{bed(N_2)}{:}T_{bed(N_{49})}\right) \quad \text{Eq. (28)}$$

4. Experiment and Model Validation

4.1 Experimental Setup and Procedure

Test facility: The adsorption and regeneration performance of MFBDD device (without water) employing M.S. Gel desiccant was evaluated experimentally and reported in detail in our previous studies [55, 57] using a test facility as shown in **Figure 5** [57], built at the University of Tokyo, Japan. A photograph of the test facility is provided in **Figure 6** [57]. The system consisted of a test section (MFBDD dehumidifier device), a gas mass flow meter (Azbil Corporation, CMS Series) to measure the incoming air flow rate, two humidity sensors (Rotronic HYGROLOG-HL-NT3), and a differential pressure gauge (OMRON ZN-DPX21-S). A humidity controller (Kotohira KTC-Z02A) was used to supply inlet air at desired temperature and humidity. A three-way valve was used to regulate the air flow from the humidity controller to the test section, which facilitated by-passing of the air heater during adsorption. The test section was placed inside a constant-temperature oven (Yamato, DKN 402, temperature range 10-260 ℃) to precisely control the ambient temperature and the whole test facility was insulated to avoid heat loss to the ambient during the regeneration experiment. An air heater was used to supply hot air during the regeneration process, and the temperature of the air heater was controlled using a proportional-integral-derivative (PID) controller.

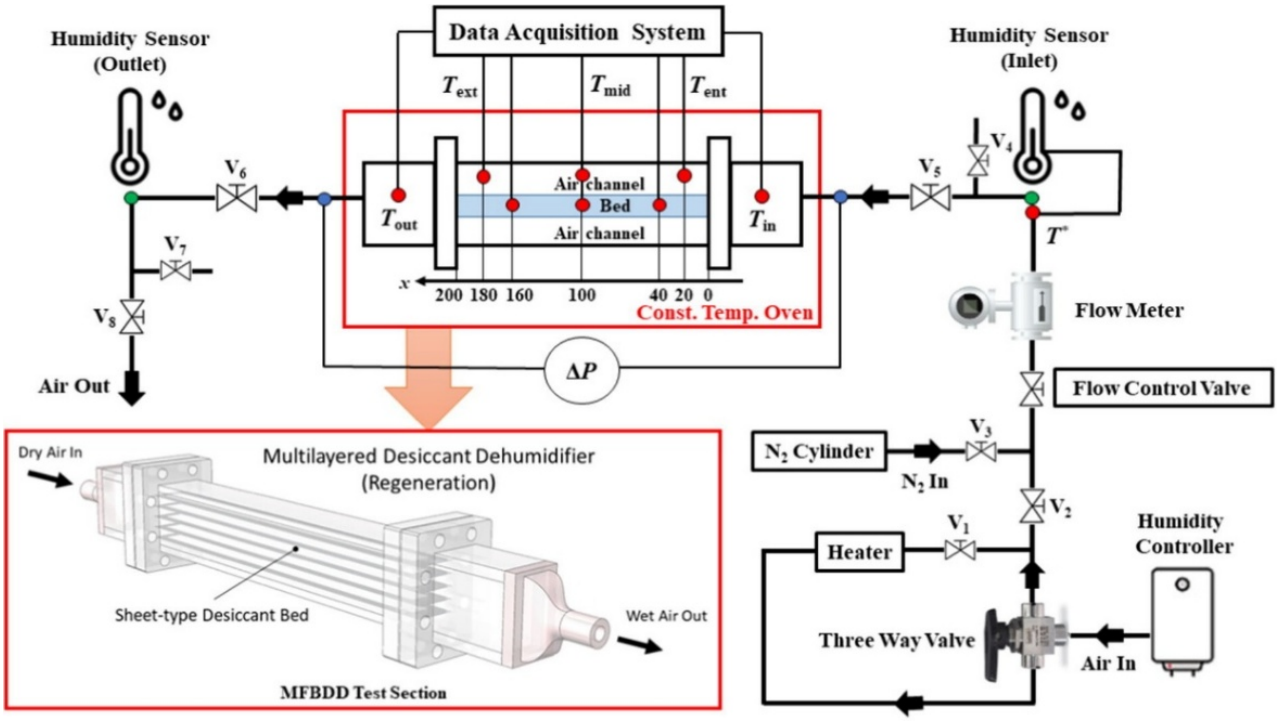

Figure 5. Schematic of the test facility used in the experimental adsorption and regeneration performance assessment of MFBDD device [57].

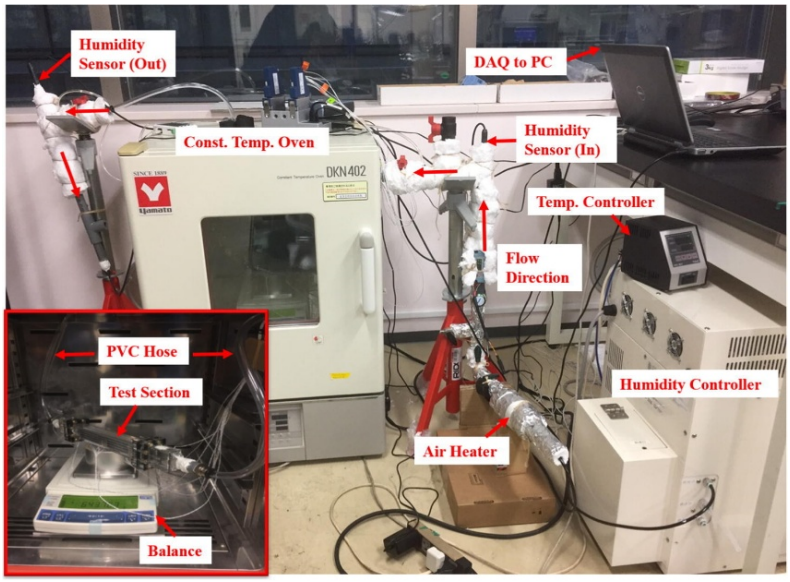

Figure 6. Photograph of the test facility used in the experimental adsorption and regeneration performance assessment of MFBDD device [57].

Sensor locations and data acquisition: Eight K-type thermocouples were installed at various locations in the test section as illustrated in **Figure 5** to record the local desiccant bed and air temperatures. To ensure precision of temperature data, all the thermocouples were calibrated using constant temperature calibration bath. The inlet and outlet temperatures of air (T_{air_in} and T_{air_out}, respectively) were recorded at the inlet and outlet plenums of the test section, respectively. For the adsorption experiments, both air and bed temperatures inside the device were recorded at x= 0.012 m, 0.10 m and 0.188 m from inlet towards outlet. For the regeneration experiments, thermocouple positions were slightly modified, the bed temperatures were recorded at an axial distance x = 0.04 m, 0.10 m and 0.16 m; and air temperatures were recorded at x = 0.02 m, 0.10 m and 0.18 m from inlet to outlet. A National Instrument (NI) compact USB data acquisition system (NI cDAQ-9174) with 8-channel thermocouple input module (NI-9219) powered by LabVIEW was used to record the transient bed and air temperatures at a 1 s interval. Inlet and outlet air humidity and pressure drop data were recorded at an interval of 5 s using distinct data loggers provided by the manufacturers of the respective sensors.

Test procedure: The details of the experimental test procedures during adsorption and regeneration experiments are provided in our previous studies [55, 57]. The adsorption experiment comprised of the following two steps [55]: (i) drying the M.S. Gel bed using dry Nitrogen (N_2) gas at room temperature, and (ii) supplying the wet air at desired humidity and temperature from the humidity controller to the test section via inlet plenum, which was an empty space at the upstream of the test section to ensure uniform distribution of the incoming air through all the desiccant layers. Dry N_2 gas was used in step (i) to precisely control the initial condition of the desiccant bed before each experimental run. During the experiment, moist air flowed over the desiccant beds, adsorption occurred, and the dry warm air appeared at the outlet of the test section. The constant temperature oven was not in operation during adsorption experiments.

Unlike adsorption experiment, the regeneration experiment comprised of six steps as illustrated in **Figure 7** [57]. The first two steps included drying of the desiccant bed using N2 gas, then adsorption at

room temperature to ensure the same initial mass of water accumulated in the bed prior to each experimental runs [57]. After that hot air was supplied to the test section under a wide range of conditions to evaluate the regeneration capacity of the bed in different conditions. Following hot air regeneration, the desiccant bed was cooled down and a second adsorption was conducted to understand the effect of different regeneration conditions on the following adsorption process.

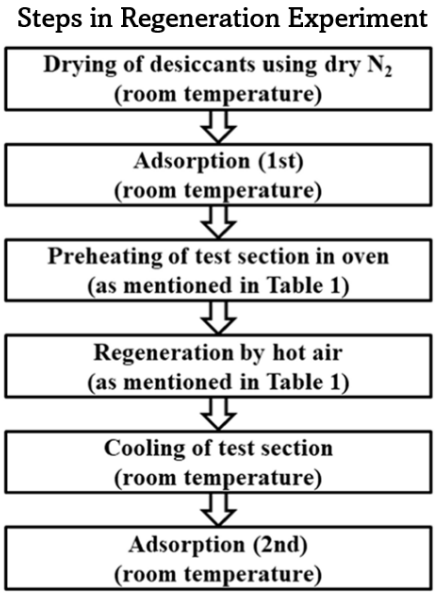

Figure 7. Flowchart showing the steps included in the experimental regeneration performance evaluation of the MFBDD device [57].

Test conditions: The details of the experimental conditions during adsorption and regeneration processes are also provided in our previous studies [55, 57]. In the original studies a wide range of conditions were investigated including varying air inlet humidity, inlet velocity and desiccant bed thickness. However, in the present study air velocity was maintained constant at 0.9 ms^{-1} during both adsorption and regeneration experiments. This velocity was chosen based on the ASHRAE Standard 55-2021: Thermal Environmental Conditions for Human Occupancy, which states that the upper limit of average air speed should be 0.8 ms^{-1} for air temperatures above 25.5°C to ensure occupants' thermal comfort. During adsorption three different humidity mixing ratios (10.01 g kg^{-1}, 14.87 g kg^{-1}, and 23.19 g kg^{-1}) were chosen for in the inlet air. The respective air inlet temperatures and air relative humidities are provided in **Table 4**. These humidity mixing ratios were chosen to cover a wide range of humidity conditions (from very high, medium and low) during the performance evaluation. During regeneration, humidity mixing ratio and air temperature at the inlet were kept constant at 8.0 g kg^{-1} and 325 K, representing 9.52 % relative humidity.

Table 4. Inlet air humidity mixing ratio, temperature and relative humidity during adsorption experiment

Humidity Mixing Ratio (g kg^{-1})	**Air Temperature** (℃)	**Air Relative Humidity %**
10.01	26.49	46.8%
14.87	26.21	70.5%
23.01	28.31	96.7%

Uncertainty analysis: The details of the uncertainty estimation including uncertainty of sensors and measured data during adsorption and regeneration experiments are provided in our previous studies [55, 57]. In summary, the propagated uncertainty, ∂U_P was estimated using Eq. (29), where ∂U_E is the uncertainty is associated with the repeatability of the experiment, and ∂U_I is the uncertainty associated with the measuring instruments.

$$\partial U_P = \sqrt{\partial U_E{}^2 + \partial U_I{}^2} \tag{29}$$

The magnitude of ∂U_E in the current study is ±5% based on the repetitive measurement data provided in **Figures 8(a)-(d)**. The magnitude of ∂U_I for different sensors used in the experiment are provided in **Table 5**. The propagated uncertainty for mass of adsorbed/desorbed and bed/air temperature were 5.06% and 5.05%, respectively, based on the Eq. (29).

Table 5. Operating range and accuracy of the sensors used in the experiment

Sensor Name	Manufacturer and Model	Operating Range	Accuracy
Mass flow meter	Azbil Corporation (CMS Series)	0-50 $Lmin^{-1}$	±3%
Differential Pressure Sensor	OMRON (ZN-DPX21-S)	±500 Pa	±3%
[1]RH sensor	Rotronic (HL-NT3)	-10 to 60 ℃; 0-100% RH	±0.1 ℃; ±0.8% RH
K-Type Thermocouples	National Instruments	0-482 ℃	±2.2 ℃ or ±0.75%

[1]RH: Relative Humidity

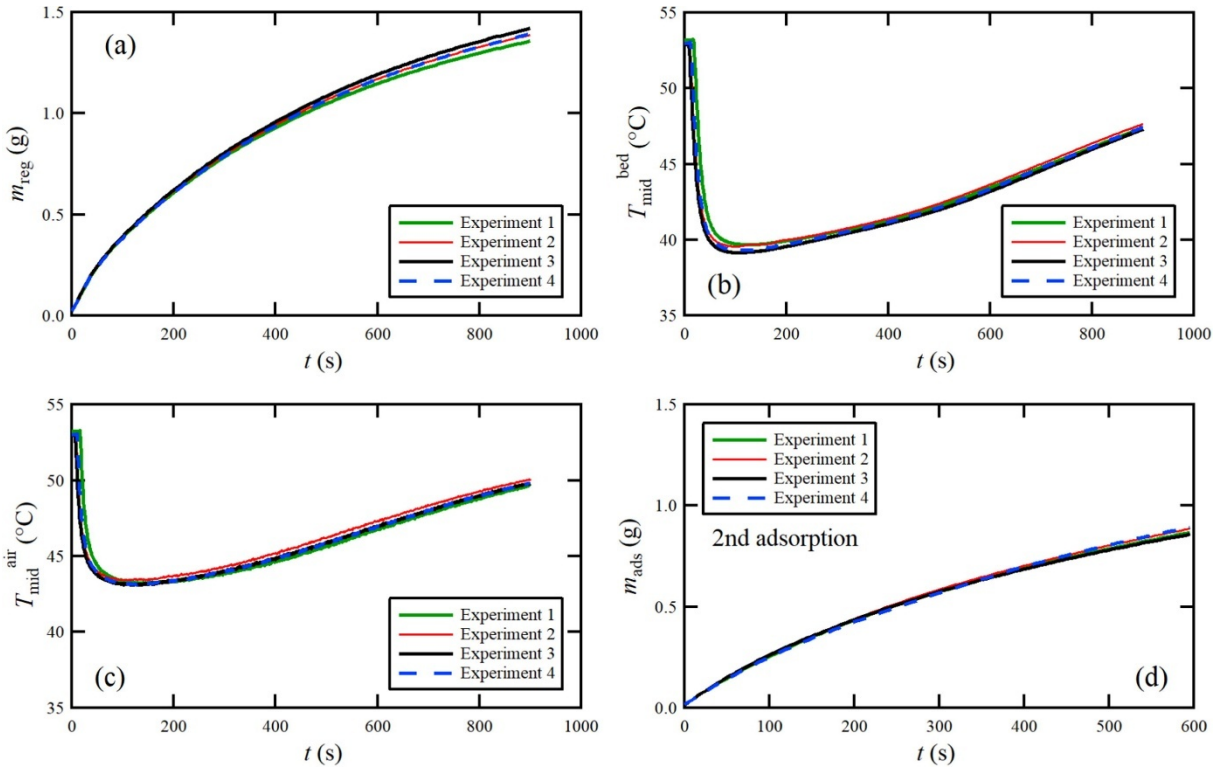

Figure 8. [57] Here, m_{reg} is the mass of water desorbed from the bed during regeneration, T_{mid}^{bed} is the bed temperature recorded at the middle (x=0.1 m), T_{mid}^{air} is the air temperature recorded at the middle (x=0.1 m), and m_{ads} is the mass adsorbed in the bed during 2nd stage adsorption as illustrated earlier in Figure 7.

4.2 Model Validation: Adsorption

The developed 1D model was validated against adsorption experiment data obtained from our previous study with the MFBDD device (without water channel) [55] and also compared with results from a previously published CFD model by Hsu et al. [56]. The inlet boundary conditions used in this case for humid air specific humidity, velocity and temperature are 0.0148 $kg\,kg_{DA}^{-1}$, 0.9 ms^{-1}, and 300 K respectively. The desiccant bed was assumed to be at 300 K initially. The ambient temperature was assumed to be constant at 300 K. As shown in **Figure 9a**, the predicted total mass of water vapor adsorbed over time (red solid line) closely matches the MFBDD experimental results (blue solid line). The model deviations remain within a margin of ±6% (gray shaded area), when compared to both the MFBDD experiment and Hsu's CFD model (dash black line). Similarly, in **Figure 9b**, the DC ($g\,kg_{DA}^{-1}$) predicted by the 1D model aligns well with the experimental data and Hsu's CFD results throughout the adsorption cycle, maintaining deviations within 10% (gray shaded area). The spatial distribution of humid air specific humidity versus time at three distinct locations (inlet, middle and outlet) is shown in **Figure S4** in the SI.

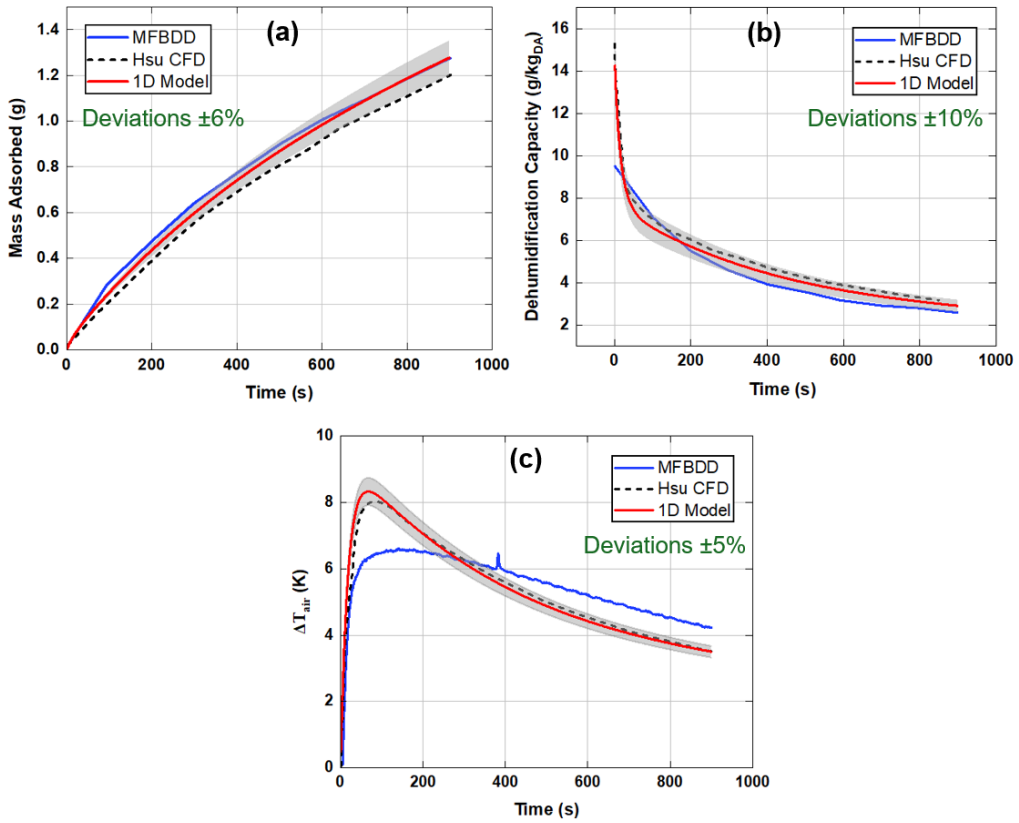

Figure 9. 1D model validation results for adsorption (without water) against MFBDD experiment data [55] and CFD model data of Hsu et al. [56]. Comparisons of (a) mass adsorbed, (b) dehumidification capacity and (c) air temperature difference between inlet and outlet of the dehumidifier device. (inlet and initial conditions: $W = 14.8\ g\ kg_{DA}^{-1}$, $u_{air} = 0.9\ ms^{-1}$, $T_{air\_in} = 300\ K$, $T_{bed} = 300\ K$, $T_{amb} = 300\ K$).

Figure 9c presents the air temperature difference (ΔT_{air}) between the outlet and inlet, where the 1D model successfully captures the Hsu's CFD results with reasonable accuracy, remaining within a ±5% margin (gray shaded area). However, both the 1D model and the CFD model fall short in accurately

reproducing the experimental ΔT_{air} observed in the MFBDD system. This discrepancy arises primarily due to the assumption of a constant convective heat transfer coefficient between the air and the desiccant bed (h_{sa}). Capturing the dynamic behavior of ΔT_{air} in the MFBDD experiment requires incorporating a time-dependent h_{sa}, which will be discussed in the next section. Overall, the 1D model demonstrates strong predictive capability with respect to key performance indicators, validating its suitability for simulating the coupled heat and mass transfer phenomena in the MFBDD system.

"To be noted that experimental validation of present 1D model under water-cooled conditions in MFBDD device is not feasible as the current device and test facility cannot be modified for chilled water circulation. In the current model, adsorption of water vapor in the bed is mainly governed by the following key parameters which are same for the beds without and with internal cooling: interparticle porosity of the bed, adsorption rate constant, and adsorption isotherm of the desiccants. Adding the equation of water circulation in the energy balance only facilitates additional heat transfer between the bed and circulating water, which reduces the desiccant bed temperature and leads to a higher dehumidification performance. Thus, water circulation does not directly affect the key parameters involved in adsorption of water vapor in the bed, and hence this should not affect the predictive nature of 1D model. This approach was also adopted in our previous performance optimization study of the MFBDD device [61].

4.2.1 Time-dependent Convective Heat Transfer Coefficient for Adsorption

Figure 10 demonstrates the capability of the 1D model to capture the experimental ΔT_{air} of the MFBDD device when a time-dependent convective heat transfer coefficient $h_{sa}\ (t)$ is incorporated into the energy equations for air (Eq. (2)) and dry desiccant bed (Eq. (4)). The time-dependent behavior of h_{sa} is simulated using the following empirical expression:

$$h_{sa}(t) = p(1 - e^{(-qt)+r})+\mathrm{s} \qquad \text{Eq. (30)}$$

In the above equation, t is the time, and $p = 10$, $q = 0.0013$, $r = 0.05$, and $s = 4.7$, are the fitting parameters. This expression provides a physically meaningful evolution of $h_{sa}(t)$, starting from an initial value and asymptotically approaching a maximum (**Figure 10a**).

Figure 10b compares the predicted ΔT_{air} after incorporating $h_{sa}(t)$ in 1D model (red line) against experimental MFBDD data (blue line). With the time-varying $h_{sa}(t)$, the 1D model accurately captures the transient behavior of ΔT_{air}, consistently staying within the ±5% range (gray shaded area) of the experimental data. This result confirms that incorporating a time-dependent convective heat transfer coefficient significantly improves the model's ability to simulate realistic thermal behavior in the MFBDD system.

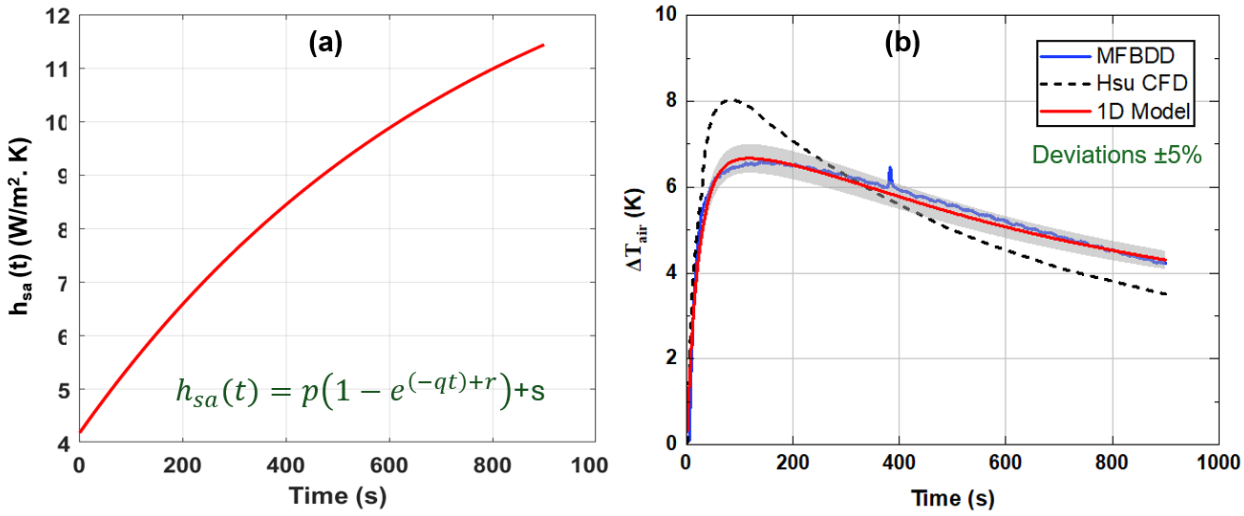

Figure 10. Comparison of air temperature difference (ΔT_{air}) between inlet and outlet of MFBDD device obtained by 1D model (present study) when time-dependent convective heat transfer coefficient ($h_{sa}(t)$) is considered between the bed and air. (a) The time-dependent profile of $h_{sa}(t)$ and the corresponding equation used to obtain the profile, and (b) the comparison of ΔT_{air} obtained by using the time-dependent $h_{sa}(t)$ in the 1D model. The 1D model successfully captures the experimental data of ΔT_{air} when the time-dependent $h_{sa}(t)$ is used. Inlet and initial conditions considered in this comparison are: $W = 14.8\ g\ kg_{DA}^{-1}$, $u_{air} = 0.9\ ms^{-1}$, $T_{air\_in} = 300\ K$, $T_{bed} = 300\ K$, $T_{amb} = 300\ K$.

Figures 11(a) and 11(b) compare the time course of mass adsorbed in the bed and dehumidification capacity, respectively for the cases when $h_{sa}$was treated as constant and as a function of time. The comparison reveals that the variations in mass adsorbed and dehumidification capacity remain within ±5% and ±6% (gray shaded region), respectively, when h_{sa} is considered time-dependent relative to the constant h_{sa} case. Hence, to simplify the modeling framework without significant loss of accuracy, the constant h_{sa} was adopted for the rest of the parametric study, consistent with our previous modeling studies [56, 61].

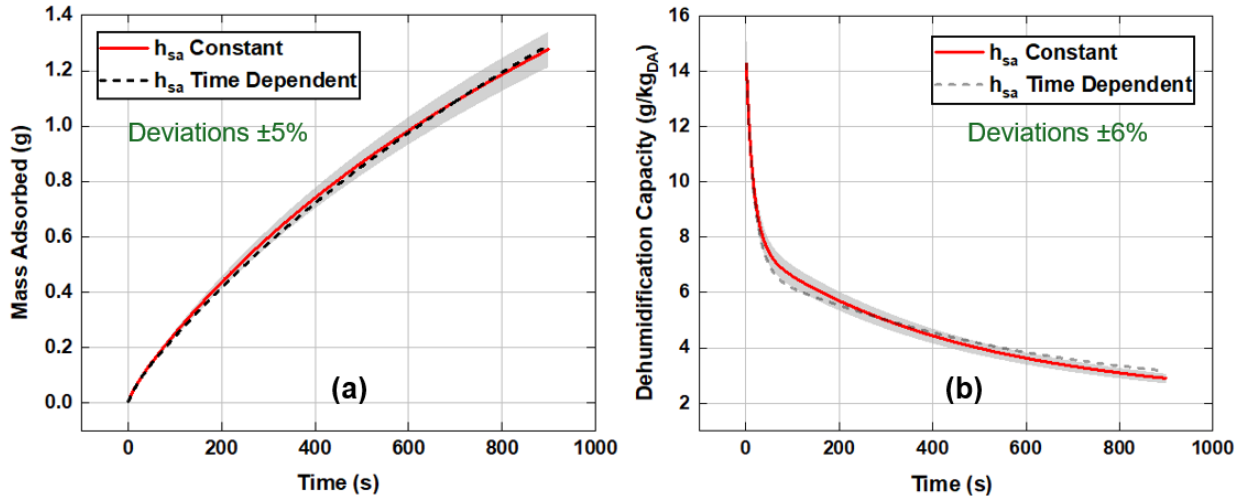

Figure 11. Comparison of (a) mass adsorbed and (b) dehumidification capacity obtained by 1D model for the cases when h_{sa} treated as constant and as a function of time.

4.2.2 Spatial Distribution of Desiccant Bed and Air Temperature: Limitation of the 1D Model

The spatial distribution of air temperature and desiccant bed temperature during the adsorption process at three axial locations (T_{air_in} and T_{bed_in} at x= 0.012 m, T_{air_mid} and T_{bed_mid} at 0.1 mm, and T_{air_out} and T_{bed_out} at 0.188 m) predicted by the 1D model is compared against Hsu's CFD results and MFBDD experiment results. **Figures 12a-c** show the air temperature comparisons at the respective locations, and **Figures 13a–c** present the corresponding desiccant bed temperature comparisons. The results indicate that for the air temperature, 1D model exhibits better accuracy than CFD model. For instance, the deviations between 1D model and experiment lies within ±0.5% (gray shaded area in **Figures 12a-c**), while the deviations between CFD results and experiment lie within ±1% (pink shaded area in **Figures 12a-c.**). The qualitative trend of the air temperatures obtained from the experiment (i.e., air temperature gradually increases from inlet to outlet) is captured by both 1D model and CFD model in this case.

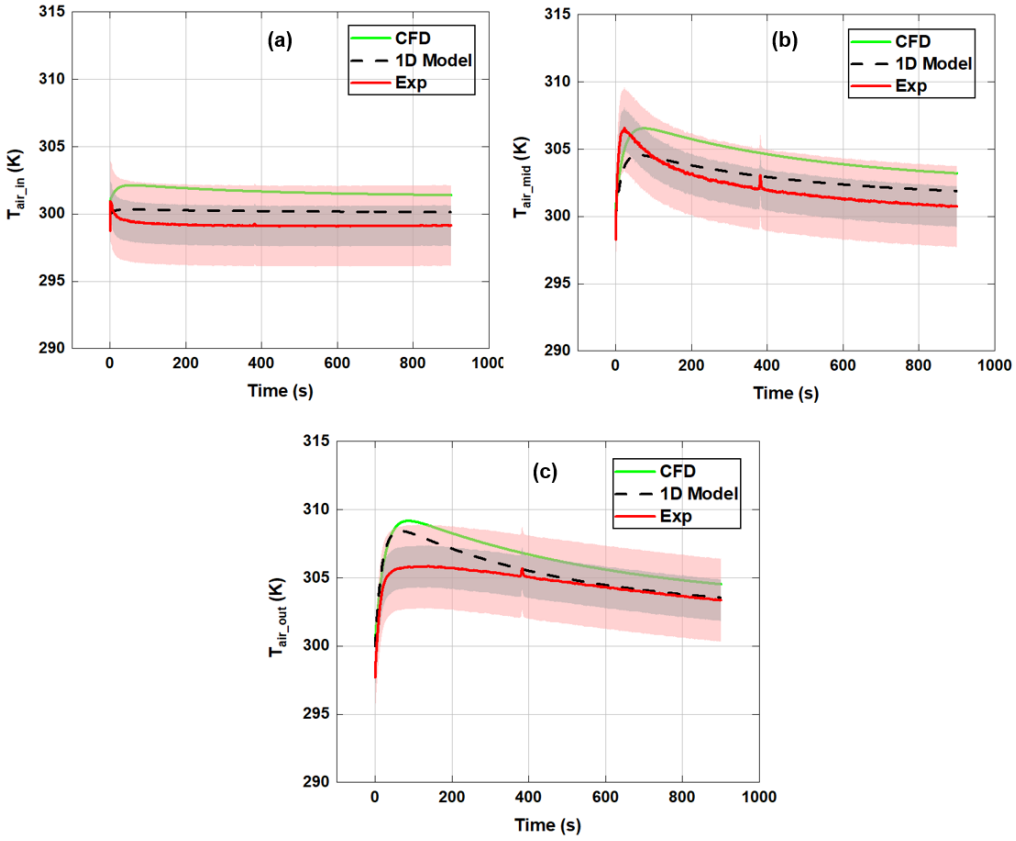

Figure 12. Air temperature distributions obtained by 1D model and compared against CFD model and MFBDD experiment results [56] during the adsorption process. (a) T_{air_in} at x = 0.012 m, (b) T_{air_mid} at x = 0.10 m and (c) T_{air_out} at x= 0.188 m. The pink and gray zones indicate ±1.0% and ±0.5% deviations respectively, using experiment results as baseline. The inlet and initial conditions are: $W_{in} = 14.8\ g\ kg_{DA}^{-1}$, $u_{air} = 0.9\ ms^{-1}$, $T_{air\_in} = 300\ K, T_{bed} = 300\ K, T_{amb} = 300\ K$.

For the bed temperature, both 1D model and CFD model exhibit larger deviation as compared to the cases of air temperature. However, near the inlet the deviation between 1D model and experiment is smaller (±4.5%, gray shaded area in **Figure 13a**), as compared to the deviation between CFD and experiment (±6 %, green shaded area in **Figure 13a**). At middle and near outlet the deviations lie within

±3% (pink shaded area in **Figures 13b-c**) for both 1D model and CFD model when compared to the experiment. Thus, in terms of the deviation margin, 1D model performs slightly better than the CFD model.

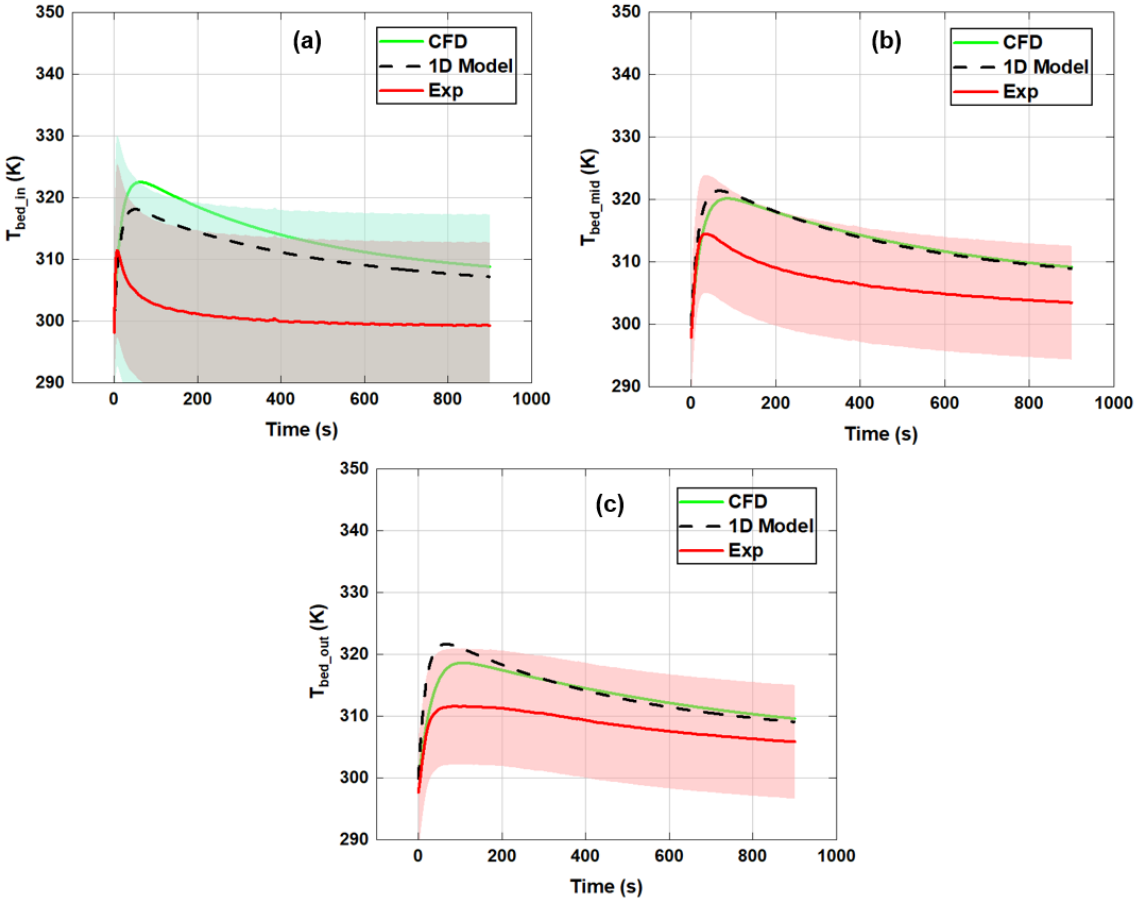

Figure 13. Bed temperature distributions obtained by 1D model and compared against CFD model and MFBDD experiment results [56] during the adsorption process. (a) T_{air_in} at x = 0.012 m, (b) T_{air_mid} at x = 0.10 m and (c) T_{air_out} at x= 0.188 m. The green and gray zones in panel (a) indicate ±6.0% and ±4.5% deviations respectively, and the pink zone in panel (b) and (c) indicates ±3.0% deviations, using experiment results as baseline. The inlet and initial conditions are: $W_{in} = 14.8\ g\ kg_{DA}^{-1}$, $u_{air} = 0.9\ ms^{-1}$, $T_{air\_in} = 300\ K, T_{bed} = 300\ K, T_{amb} = 300\ K$.

However, to be noted that the trend of local bed temperature in MFBDD experiment was as follows: the peak bed temperature appeared at the middle (T_{bed_mid}), followed by T_{bed_out} and T_{bed_in} as shown in **Figure 14a**. In the case of CFD results (**Figure 14b**), the bed temperature was highest at the inlet, followed by T_{bed_mid} and T_{bed_in}. In the case of 1D model results (**Figure 14c**), the peak bed temperature was highest at the outlet, T_{bed_mid} was nearly identical to T_{bed_out} and T_{bed_in} was the smallest. Thus, both CFD and 1D model failed to accurately predict the trend of local bed temperatures in the experiment. This discrepancy arises because both models assume a uniform porosity of the desiccant bed along the axial direction, whereas this assumption may not hold true in the actual MFBDD device. During the experiment, the incoming airflow caused slight movement of the desiccant particles toward the middle of the bed due to the binder-free configuration. As a result, the bed porosity near the inlet region became relatively higher,

leading to a smaller amount of desiccant material and consequently a minimal temperature rise in this region during the experiment.

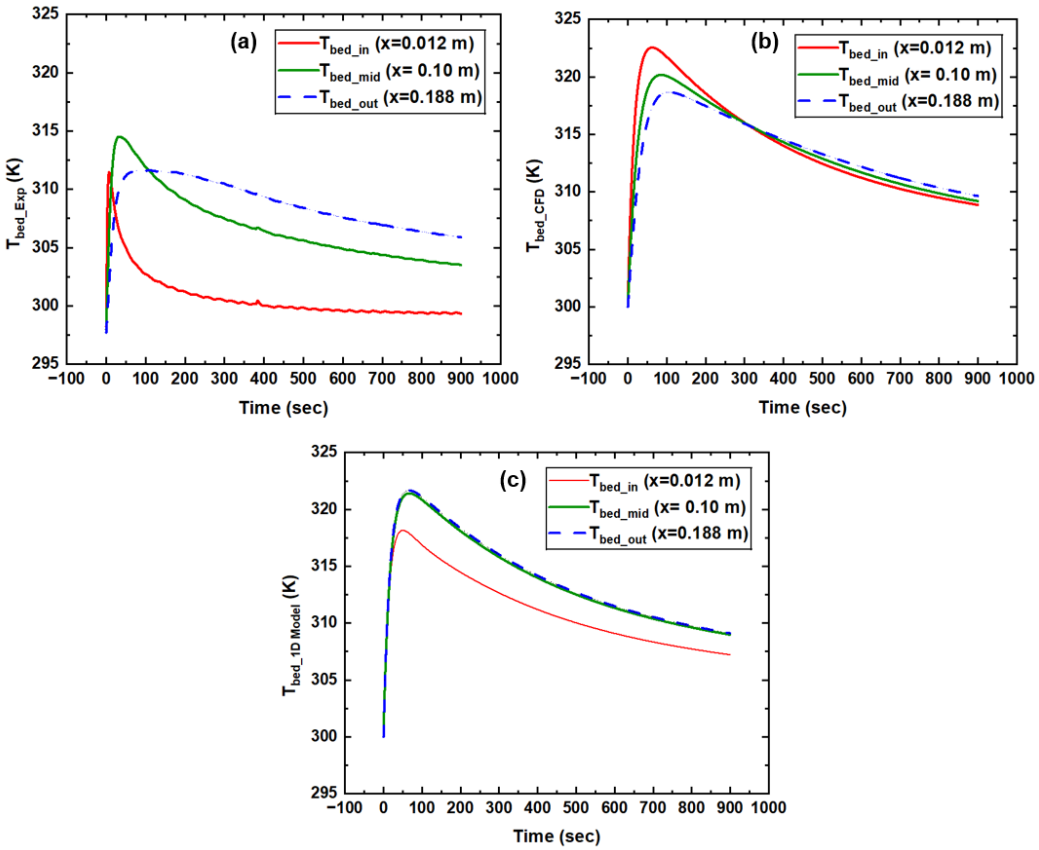

Figure 14. Comparisons of local bed temperature distributions. (a) MFBDD experiment [55], (b) CFD results of Hsu et al. [56] and (c) present 1D model. The inlet and initial conditions are: $W_{in} = 14.8\ g\ kg_{DA}^{-1}$, $u_{air} = 0.9\ ms^{-1}$, $T_{air\_in} = 300\ K$, $T_{bed} = 300\ K$, $T_{amb} = 300\ K$.

From **Figures 14b and 14c**, one can also observe that the trend of local bed temperature as predicted by the 1D model is opposite to that observed in the CFD results: the 1D model shows an increasing bed temperature from inlet to outlet, whereas CFD results show a decreasing trend along the axial direction. During the operation of the MFBDD system, the majority of water vapor adsorption occurs within the initial few tens of seconds. As adsorption progresses, the mass transfer zone advances from the inlet toward the outlet due to gradual saturation of the desiccant material. Consequently, the majority of the enthalpy of adsorption is released near the inlet at the onset of adsorption. Thus, a higher desiccant bed temperature near the inlet physically reasonable for a bed with uniform porosity in the axial direction. However, in the current 1D model, the adsorption kinetics is governed by the average specific humidity of air (W_{avg}) and average bed temperature ($T_{bed,\,avg}$) across the spatial domain, as used in Eqs. (9) and (10) to estimate P_{sat} and P_v, respectively. This modeling approach is based on the lumped parameter method used by Lili et al. [5] in their performance optimization study of the MFBDD system. Attempts to implement local values of air specific humidity and bed temperature in these equations led to numerical instability, with MATLAB's ode23s solver unable to satisfy integration tolerances. As a result, the primary limitation of the present 1D

model lies in its inability to resolve the trend of local desiccant bed temperatures during transient adsorption processes.

To be noted that the local temperature distributions are useful to understand the underlying adsorption mechanism in the desiccant bed. However, ΔT_{air} between outlet and inlet are more important for system design consideration, as this is directly related to the cooling load in the next stage to ensure occupants' thermal comfort when a desiccant dehumidifier is intended to use in hybrid air conditioning system. As discussed earlier in **Figure 9c**, 1D model could successfully capture ΔT_{air} within ±5% deviations. Hence, the inability of 1D model to capture the trend of local bed temperature distribution will not lead to significant errors in system design.

To compensate for this inability of the 1D model to capture the trend of local bed temperature distributions, we compared the mean desiccant bed temperature predicted by the 1D model with that obtained from Hsu's CFD model, as shown in **Figure 15**. Despite the simplifications inherent in the 1D approach, the model demonstrates excellent agreement in terms of mean bed temperature, with a deviation of only ±0.3% (gray shaded area) from the CFD results. This strong alignment suggests that, while the 1D model cannot resolve spatial variations, it remains highly effective in predicting overall thermal behavior of the MFBDD device.

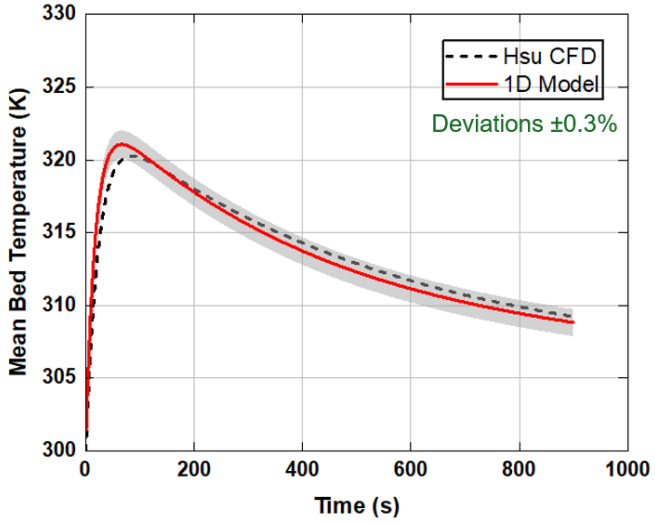

Figure 15. Comparison of mean desiccant bed temperatures obtained by 1D model (present study) and CFD model of Hsu et al. [56]. The inlet and initial conditions considered in this comparison are as follows: $W_{in} = 14.8\ g\ kg_{DA}^{-1}$, $u_{air} = 0.9\ ms^{-1}$, $T_{air\_in} = 300\ K$, $T_{bed} = 300\ K$, $T_{amb} = 300\ K$)

4.3 Model Validation: Regeneration

Upon validation of the adsorption part, the developed 1D model was also validated against the regeneration experiment and CFD results obtained from our previous studies [57, 58]. The inlet boundary conditions used in this case for humid air specific humidity, velocity and temperature are 0.008 $kg\ kg_{DA}^{-1}$, 0.9 ms^{-1}, and 325 K, respectively. The desiccant bed was assumed to be at 325 K initially. The ambient temperature was assumed to be constant at 327 K.

As shown in **Figure 16a**, the predicted total mass of water vapor desorbed over time (red solid line) closely matches the MFBDD experimental results (blue solid line). The 1D model remains within a ±5% margin, as illustrated by the gray shaded area, when compared with experimental data. In **Figure 16b**, the predicted regeneration capacity also shows good agreement with experimental values; however, the deviation increases to as much as ±15% (gray shaded area). This larger discrepancy is attributed to the complex heat and mass transfer phenomena inherent in the regeneration process, which is discussed in more detail in our CFD modeling study [58]. Despite this, the 1D model demonstrates better accuracy compared to the CFD model in predicting both the total mass of water vapor desorbed and the regeneration capacity over time. Additionally, the spatial distributions of air specific humidity, desiccant bed temperature, and air temperature during the regeneration process are presented in **Figures S5a–S5c** in the SI. The corresponding air temperature difference ΔT_{air} between the inlet and outlet during regeneration is shown in **Figure S5d**.

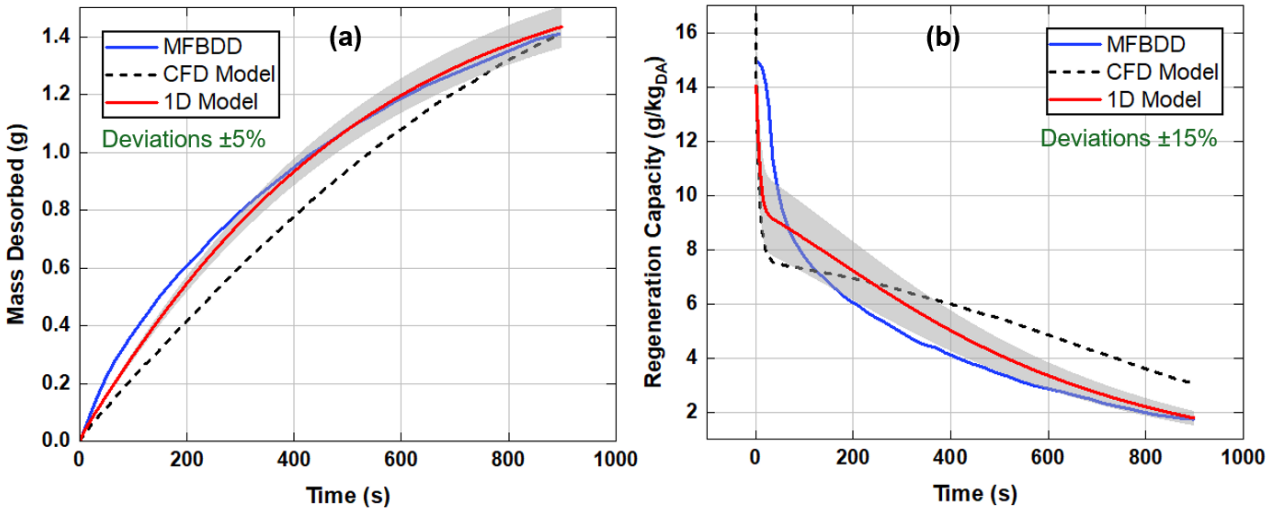

Figure 16. 1D model validation results for regeneration (without water) against MFBDD experiment data [57] and CFD model data of Shamim et al. [58]. Comparisons of (a) mass desorbed, and (b) regeneration capacity (inlet and initial conditions: $W_{in} = 8.0\ g\ kg_{DA}^{-1}$, $u_{air} = 0.9\ ms^{-1}$, $T_{air\_in} = 325\ K$, $T_{bed} = 325\ K, T_{amb} = 327\ K$).

5 Results and Discussion

5.1 Dehumidification Performance in Water-Cooled MFBDD with M.S. Gel

Influence of inlet specific humidity of air: Following model validation, the developed 1D model was applied to predict the adsorption performance of the MFBDD device with internal cooling under various operating conditions. **Figures 17a and 17b** illustrate the total mass of water vapor adsorbed and the *DC*, respectively, for the M.S. Gel bed, both without internal cooling (dashed lines with circle markers) and with internal cooling (solid lines), across a range of inlet specific humidity values from 10.0 – 23.0 $g\ kg_{DA}^{-1}$. The corresponding air temperature difference between inlet and outlet (ΔT_{air}) is presented in **Figures 17c.** To be noted that the data for M.S. Gel bed without internal cooling are taken from our previous experimental study [55]. The mean bed temperature and water outlet temperature obtained by 1D model for the water-cooled cases are provided in **Figure S6a and S6b** respectively, in the supporting information. The figures clearly show that internal cooling significantly enhances both mass adsorbed and *DC* under all inlet humidity conditions. The ΔT_{air} also becomes significantly lower for the water-cooled cases. Thus,

introducing internal cooling of the bed has great potential to reduce the energy consumption for evaporative cooling of air after the dehumidification.

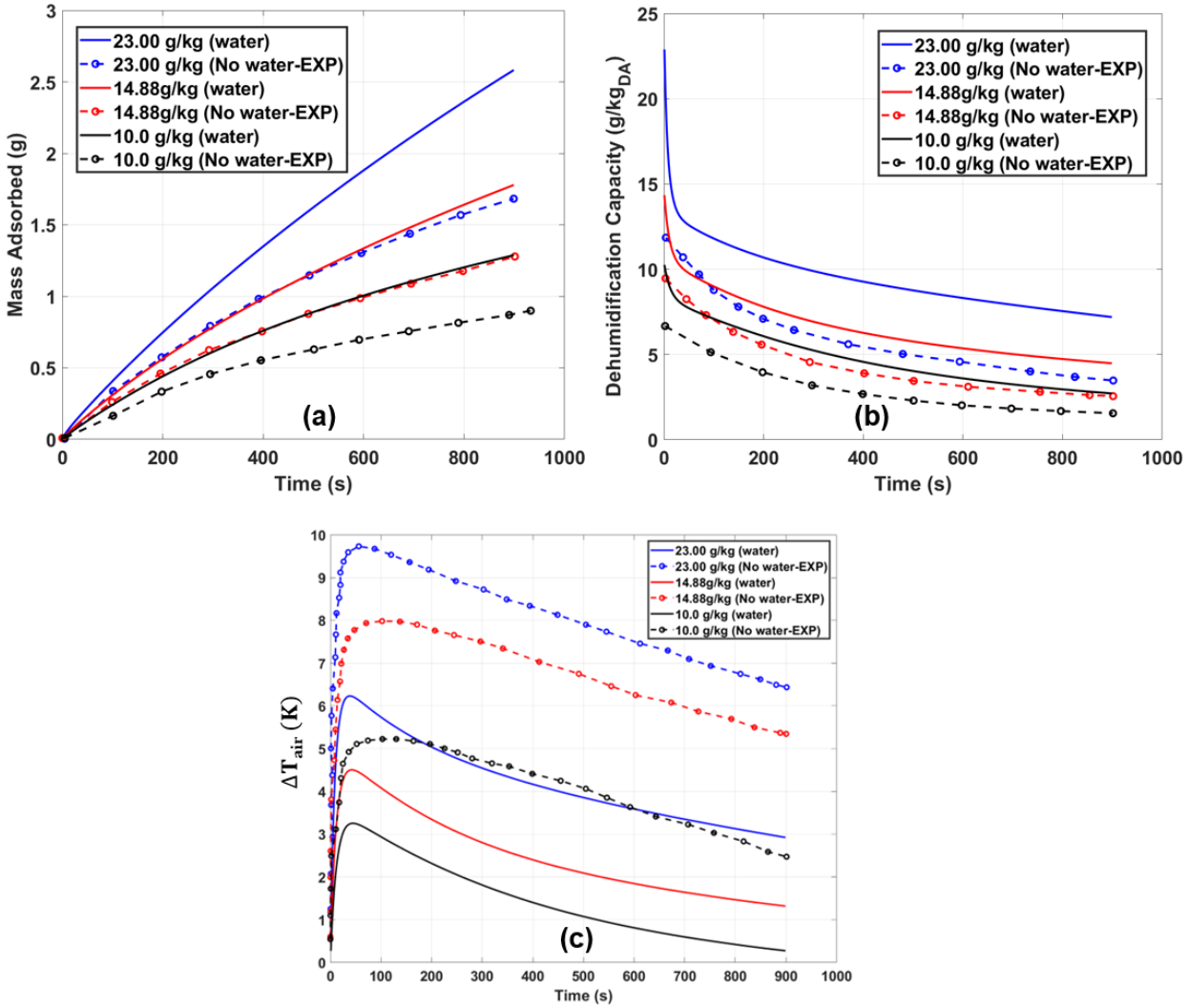

Figure 17. Comparison of dehumidification performance under different specific humidities of inlet air in MFBDD without and with internal cooling. (a) mass adsorbed and (b) dehumidification capacity, and (c) ΔT_{air} between outlet and inlet of the dehumidifier. Inlet conditions considered in this comparison are: $u_{air} = 0.9\ ms^{-1}$, $u_w = 0.8\ ms^{-1}$, $T_{air\_in} = 300\ K$, $T_{w\_in} = 293.15\ K$. Data for water-free cases are taken from [55].

(i) Influence of inlet velocity of water: Figures 18a and 18b present the total mass of water vapor adsorbed and the *DC*, respectively, for the M.S. Gel bed with internal cooling at varying inlet water velocities ranging from 0.6 – 1.0 $m\ s^{-1}$. The results indicate that both adsorption capacity and dehumidification performance improve with increasing water inlet velocity. This enhancement is primarily attributed to the rise in the convective heat transfer coefficient between the circulating water and the desiccant bed (h_{sw}) at higher inlet velocities. The associated air temperature difference between the inlet and outlet (ΔT_{air}) and mean desiccant bed temperature are shown in **Figures 18c and 18d,** respectively. Due to the enhanced mass flow rate, more heat was removed from the desiccant bed when the inlet water

velocity was highest. Consequently, ΔT_{air} and mean bed temperature were lowest in the case of highest inlet water velocity (**Figures S7a and S7c).** The corresponding water outlet temperatures for the cases with different water inlet velocity are shown in **Figure S7** in supporting information. As the water velocity increases, the heat capacity of water increases due to the enhanced mass flow rate. As a result, the water temperature at the outlet was lowest when the inlet water velocity was highest.

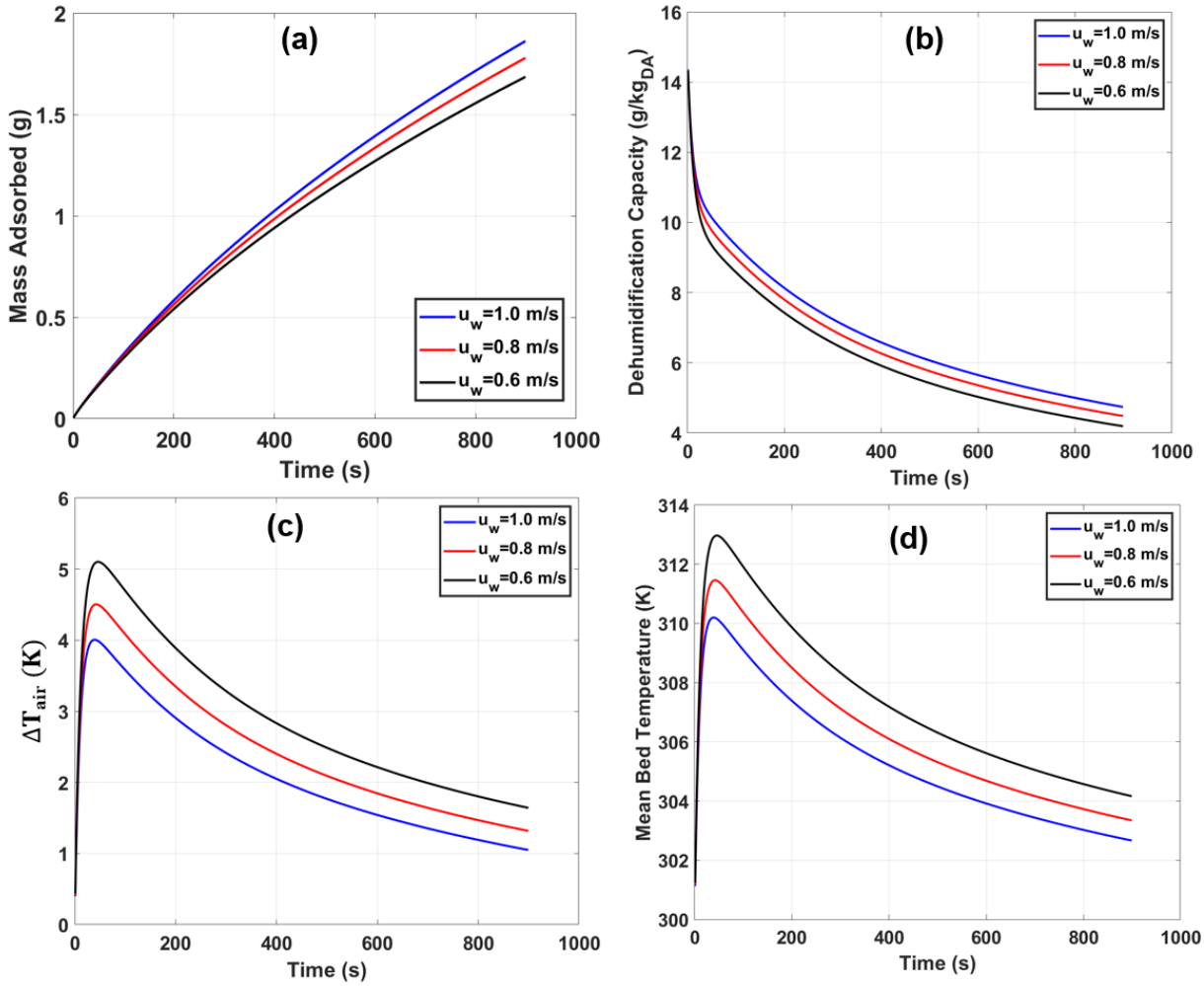

Figure 18. Comparison of dehumidification performance under different inlet velocities of chilled water in internally cooled MFBDD. (a) mass adsorbed and (b) dehumidification capacity, (c) ΔT_{air} between outlet and inlet of the dehumidifier, and (d) mean bed temperature. Inlet conditions considered in this comparison are: $W_{in} = 14.8\ g\ kg_{DA}^{-1}$, $u_{air} = 0.9\ ms^{-1}$, $T_{air\_in} = 300\ K$, $T_{w\_in} = 293.15\ K$.

(ii) Influence of the inlet temperature of water: Figures 19a and 19b present the total mass of water vapor adsorbed and the *DC*, respectively, in the M.S. Gel bed with internal cooling under varying inlet water temperatures ranging from 298.15 K to 283.15 K. As expected, both adsorption capacity and dehumidification performance improve with decreasing inlet water temperature, due to enhanced heat extraction from the desiccant bed. The corresponding air temperature difference between the inlet and outlet (ΔT_{air}) and the mean bed temperature are shown in **Figures 19c and 19d**, respectively. As the inlet water temperature decreases, both ΔT_{air} and mean bed temperature decrease, indicating more effective bed

cooling. The outlet water temperatures for all four cases are provided in **Figure S8** in the supporting information.

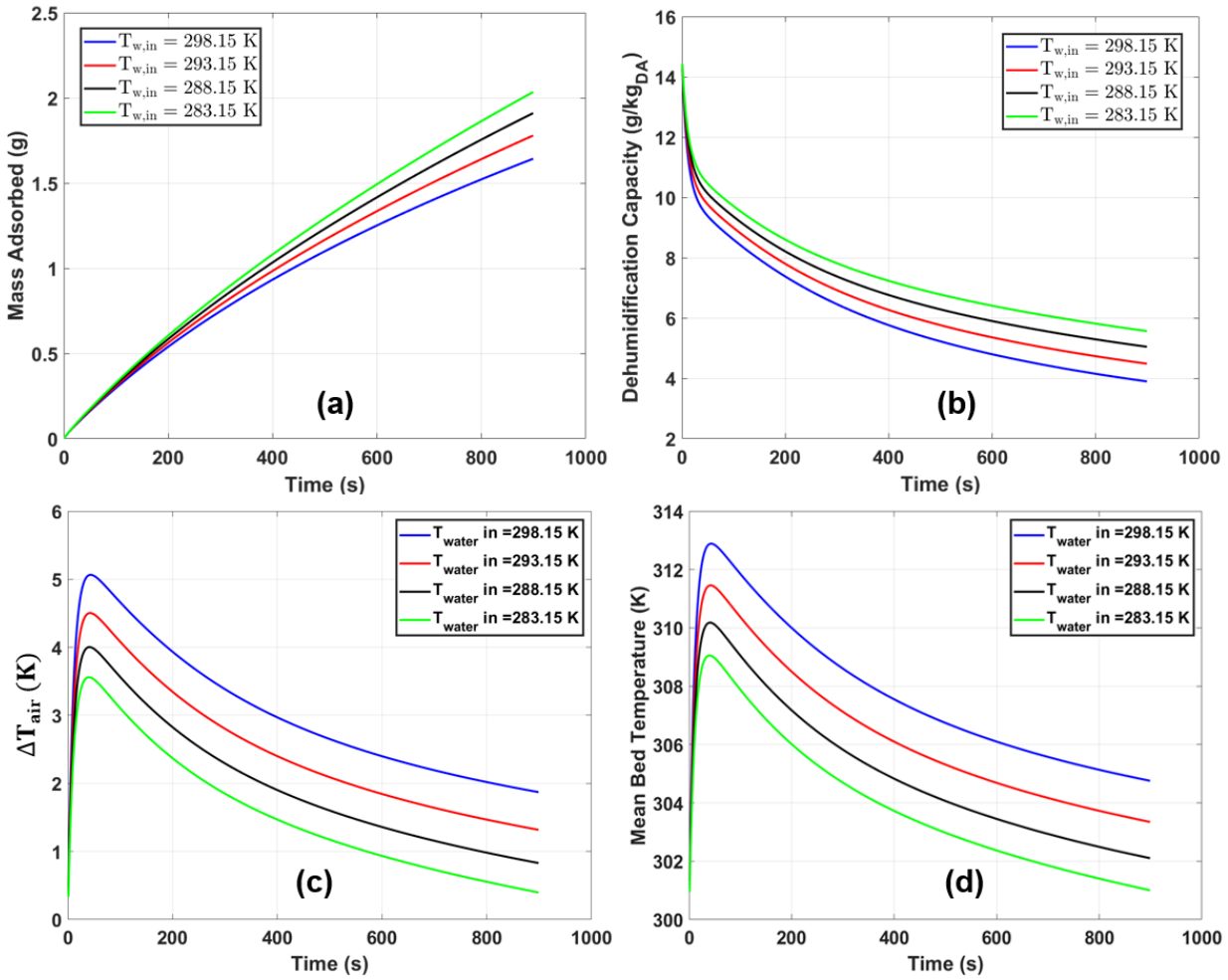

Figure 19. Comparison of dehumidification performance under different inlet temperatures of chilled water in internally cooled MFBDD. (a) mass adsorbed and (b) dehumidification capacity, (c) ΔT_{air} between outlet and inlet of the dehumidifier, and (d) mean bed temperature. Inlet conditions considered in this comparison are: $W_{in} = 14.8\ g\ kg_{DA}^{-1}$, $u_{air} = 0.9\ ms^{-1}$, $T_{air\_in} = 300\ K$, $u_w = 0.8\ ms^{-1}$.

(iii) Summary of performance enhancement with internal cooling in M.S. Gel bed

In order to summarize the moisture adsorption performance with internal cooling in M.S. Gel bed, herein, we report the percentage (%) increment of mass adsorbed, moisture removal capacity (MRC) (i.e., the cycle average dehumidification caapcity) and dehumidification effectiveness ($\epsilon_{dehum.}$) for three different adsorption cycle durations (t_{cyc} = 300s, 600s and 900s). Here, mass adsorbed (g) is the total mass of water vapor in the desiccant bed at the end of each cycle time, and estimated using previously expressed Eq. (24). MRC and ϵ_{dehum} are estimated using the following expressions:

$$MRC(g/kg_{DA}) = \frac{\int_0^{t_{cyc}}((W_{in} - W_{out}) \times 1000)\, dt}{t_{cyc}} \qquad \text{Eq. (31)}$$

$$\epsilon_{dehum} = \frac{\int_0^{t_{cyc}} \frac{(W_{in} - W_{out})}{W_{in}} \, dt}{t_{cyc}} \quad \text{Eq. (32)}$$

Finally, the above three performance indicators estimated in M.S. Gel bed with internal cooling are compared to those obtained from MFBDD experiment data (without internal cooling) as reported in [55]. For each performance indicator, we estimated the % increment under two scenarios: (1) varying the inlet specific humidities while the circulating water inlet temperature was constant at 293.15K, and (2) varying the inlet water temperatures while the inlet air specific humidity was kept constant at 23.0 $g\ kg_{DA}^{-1}$. Other operating conditions considered in scenarios (1) and (2) are as follows: $u_{air} = 0.9\ ms^{-1}$, $u_w = 0.8\ ms^{-1}$, $T_{air\_in} = 300\ K$.

Table 6 and **Table 7** report the % increment for mass adsorbed, MRC and ϵ_{dehum}, respectively, for scenarios (1), and (2), respectively. **Table S5**, **Table S6** and **Table S7** provide the absolute amount of mass adsorbed, MRC, and ϵ_{dehum}, respectively, at the end of each t_{cyc} in the M.S. Gel bed with and without internal cooling for scenario (1). **Table S8**, **Table S9** and **Table S10** provide the absolute amount of mass adsorbed, MRC, and ϵ_{dehum}, respectively, at the end of each t_{cyc} in the M.S. Gel bed with and without internal cooling for scenario (2).

According to the results presented in **Table 6** and **Table 7**, all three performance indicators (i.e., mass adsorbed, MRC, and ϵ_{dehum}) exhibit significant improvement when the M.S. Gel bed is water cooled. From **Table 7**, mass adsorbed can be enhanced by over 70% with internal cooling at 283.15 K (when t_{cyc} =900 s and W_{in} =23.0 $g\ kg_{DA}^{-1}$). Similarly, both MRC and ϵ_{dehum} can be enhanced by over 80% with internal cooling (**Table 7**) at 283.15 K (when t_{cyc}=900 s and W_{in} =23.0 $g\ kg_{DA}^{-1}$).

Also note that, under all the inlet conditions considered, the % enhancement for all three indicators increase almost linearly as the cycle duration gradually becomes longer (from 300 s to 900 s). During water vapor uptake, the release of adsorption enthalpy raises the desiccant bed temperature, leading to lower relative humidity of the air in the desiccant bed (details will be discussed later). The rise of desiccant bed temperature can be suppressed with internal cooling. As a result, the M.S. Gel bed without water circulation approaches to the saturation condition earlier than the bed with water circulation. Thus, circulating cooling water during adsorption allows the desiccant bed to maintain higher dehumidification performance over longer cycle durations.

Table 6. Percentage increment of mass adsorbed, MRC, and ϵ_{dehum} with water circulation in the M.S. Gel bed as compared to the case without water circulation ($T_{w\_in} = 293.15\ K$)

Inlet W ($g\ kg_{DA}^{-1}$)	Mass adsorbed			MRC			ϵ_{dehum}		
	300s	600s	900s	300s	600s	900s	300s	600s	900s
23.0	32.91	44.62	53.57	41.46	53.19	63.10	40.56	52.72	61.18
14.8	23.81	34.34	39.37	33.00	43.53	49.89	32.50	43.06	48.15
10.0	35.56	42.86	47.13	45.02	54.34	58.92	46.09	53.76	57.33

Table 7. Percentage increment of mass adsorbed, MRC, and $\epsilon_{dehum}$with water circulation in the M.S. Gel bed as compared to the case without water circulation ($W_{in} = 23.0\ g\ kg_{DA}^{-1}$)

T_{w_in} (K)	Mass adsorbed			MRC			ϵ_{dehum}		
	300s	**600s**	**900s**	**300s**	**600s**	**900s**	**300s**	**600s**	**900s**
293.15	32.91	44.62	53.57	41.46	53.19	63.10	40.56	52.72	61.18
288.15	40.51	52.31	63.10	47.93	61.81	73.10	46.94	61.22	71.37
283.15	45.57	60.00	71.43	53.78	69.54	82.24	52.78	69.05	80.39

5.2 Dehumidification Performance in Water-Cooled MFBDD with MIL-101/GO-6

Desiccant materials exhibiting step-shape isotherms often demonstrate higher working capacities due to their sharp water vapor uptake capacities within a narrow relative humidity range [73]. Hence, for dehumidification applications, a step-shape isotherm is generally more advantageous than an S-shape isotherm [35, 74]. MOFs are well-known for their ability to achieve high water vapor uptake with step-shape isotherms [75]. Therefore, to enhance dehumidification capacity, herein, we simulated the adsorption performance of the MFBDD device by integrating internal cooling with a composite MOF (MIL-101/GO-6) reported by Yan et al. [62] that exhibited step-shape isotherm and exceptionally high water uptake (≈1.6 g/g) within the narrow relative humidity range of 35–47% (as shown earlier in **Figure 4c**).

The simulated results for mass adsorbed, dehumidification capacity (*DC*), air temperature change (ΔT_{air}), and mean bed temperature for MIL-101/GO-6 with and without internal cooling, under various inlet temperatures and specific humidities, are presented in **Figures 20a–d**. These results are also compared with the baseline case using M.S. Gel without internal cooling. As shown in **Figures 20a and 20b**, both the mass adsorbed and *DC* can be enhanced using MIL-101/GO-6 (solid green line), relative to the M.S. Gel baseline (solid red line), even in the dry bed. However, when internal cooling is introduced to the MIL-101/GO-6 bed, the enhancements in mass adsorbed and *DC* become substantially higher (dashed lines), especially at low water inlet temperature (283.15 K) (dashed blue line). The dashed pink line represents the case when inlet specific humidity was increased to 20 $g\ kg_{DA}^{-1}$ at water inlet temperature 283.15 K.

Table 8 summarizes the % enhancement in mass adsorbed, MRC, and ϵ_{dehum} for MIL-101/GO-6 cases compared to M.S. Gel baseline without and with water circulation when $W_{in} = 14.8\ g\ kg_{DA}^{-1}$. **Table S11** provides the absolute amount of mass adsorbed, MRC, and ϵ_{dehum}, respectively, at the end of each t_{cyc} for M.S. Gel (without water) and MIL-101/GO-6 with and without cooling water at different temperatures. From **Table 8,** when MIL-101/GO-6 was employed in the dry bed, the enhancements in all three performance indicators remained modest, ranging from **6% to 19%.** In contrast, the inclusion of internal cooling with MIL-101/GO-6 led to substantial performance improvements, with enhancements reaching as high as **50%–99%** for three performance indicators. **Table 9** presents a comparison of the MRC obtained in the present study using MIL-101/GO-6 with values reported in recent literature under similar operating conditions using different MOFs. The results indicate that the MRC achieved in this study is nearly twice as high as those reported in the literature. These findings suggest that, although the step-shaped isotherm of MIL-101/GO-6 enhances dehumidification performance, the integration of internal cooling and the use of the desiccant in a binder-free configuration are critical for further performance improvements.

Table 8. Percentage Increment of mass adsorbed, MRC, and ϵ_{dehum} with MIL-101/GO-6 as compared to the case of M.S. Gel without water circulation ($W_{in} = 14.8\ g\ kg_{DA}^{-1}$)

Desiccant and conditions	Mass adsorbed			MRC			ϵ_{dehum}		
	300s	600s	900s	300s	600s	900s	300s	600s	900s
MIL-101/GO-6 (No water)	11.67	16.33	18.90	6.80	10.28	12.69	6.82	15.61	17.85
MIL-101/GO-6 ($T_{w\_in} = 293.15\ K$)	53.33	62.24	73.23	48.07	55.14	65.81	47.73	61.85	75.08
MIL-101/GO-6 ($T_{w\_in} = 283.15\ K$)	63.33	78.57	96.06	58.89	71.78	87.96	56.82	79.19	98.65

Table 9. Comparison of MRC obtained in the present study with recent literature

Ref.	Desiccant	Chilled water inlet temp. (℃)	Inlet specific humidity (g/kg_{DA})	Cycle time (min)	MRC (g/kg_{DA})
[49]	Silica gel/ MIL-100(Fe)	25	21.5	10	4.1
[50]	MIL-101(Cr)	25	19.22	12	4.6
[46]	Aluminum Fumarate	20	13	5	4.5
This work	MIL-101/GO-6	20	14.8	5/10	9.58/8.3

To elucidate the mechanism underlying the significant performance enhancement achieved with internal cooling in the MIL-101/GO-6 bed, we also analyzed the ΔT_{air} and mean bed temperature, as shown in **Figures 20c and 20d**, respectively. As observed, both ΔT_{air} and mean bed temperatures are higher for the cases without internal cooling (solid lines). In the case of dry bed, the rise in ΔT_{air} and mean bed temperature for the MIL-101/GO-6 (solid green lines) is more pronounced than the M.S. Gel (solid red lines) due to the high adsorption heat release associated with the larger water uptake capacity of MIL-101/GO-6. However, when internal cooling is applied, both ΔT_{air} and mean bed temperature (dashed lines) are significantly reduced, falling below those observed in the cases without internal cooling. A lower mean bed temperature leads to an increase in air relative humidity within the bed, which enhances the driving force for adsorption and thus results in a substantial improvement in dehumidification performance. This mechanism will be discussed in detail in the following section.

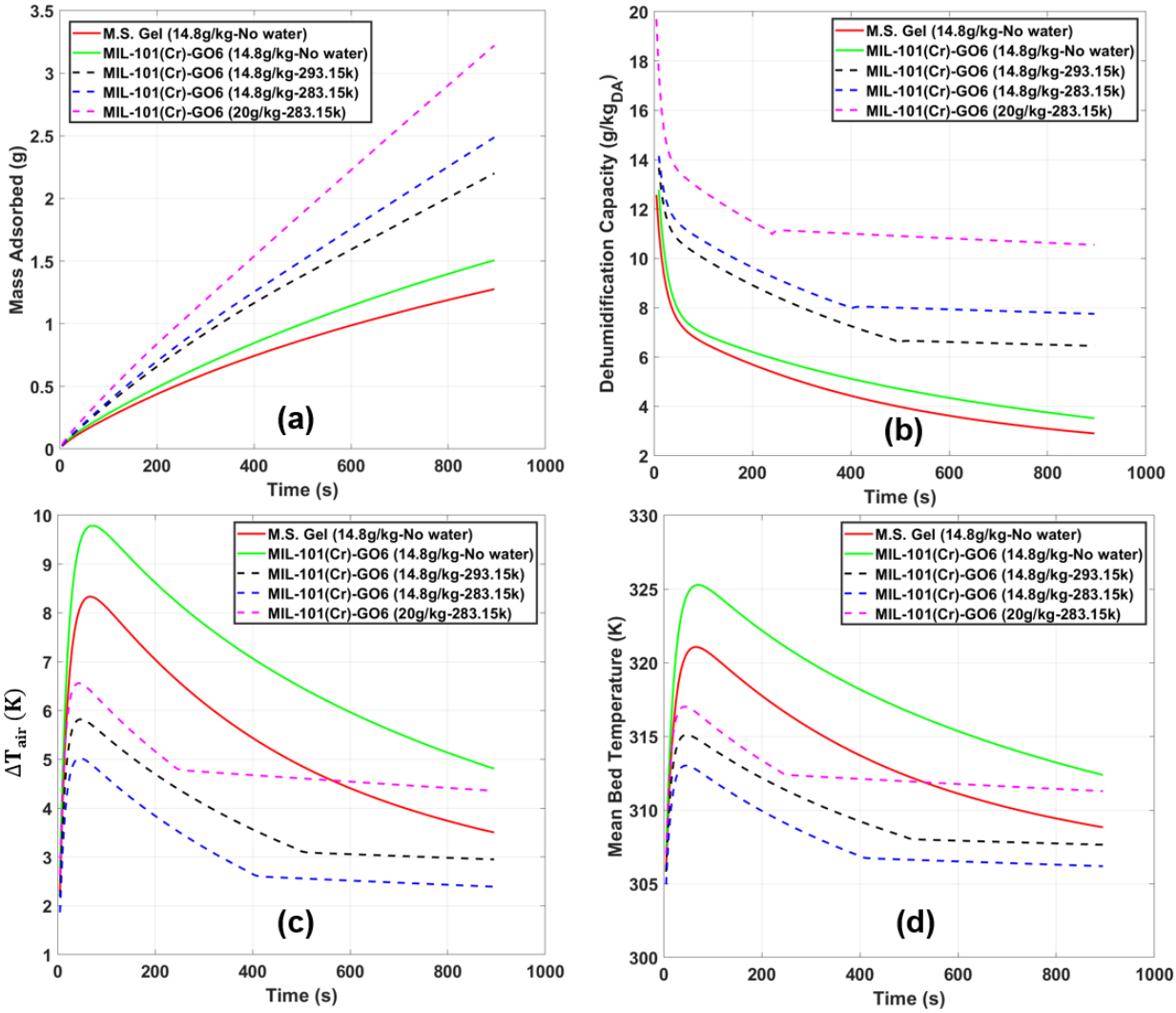

Figure 20. Comparison of mass and heat transfer characteristics during adsorption in MFBDD device when S-shape (M.S. Gel) and step-shape (MIL-101/GO-6) isotherms are considered. Results of (a) mass adsorbed, (b) dehumidification capacity, (c) air temperature difference between inlet and outlet and (d) mean bed temperature. The results show that with decreasing cooling water temperature, adsorption performance can be noticeably improved and the benefit of using step-shape isotherm becomes more obvious.

5.3 Influence of Internal Cooling on Bed Relative Humidity (φ)

To further elucidate the influence of internal cooling on enhancing dehumidification performance with MIL-101/GO-6, the time course of relative humidity of air within the bed is plotted in **Figure 21** for different cases**.** This figure reveals that, in cases without internal cooling (solid red and green lines), φ drops sharply during the early stage of adsorption, followed by a gradual recovery as adsorption progresses. The sharp initial decrease is more pronounced for MIL-101/GO-6 than for M.S. Gel, due to the higher adsorption enthalpy associated with the former. However, when internal cooling is applied (dashed black and blue lines), the decrease in φ is smaller, and the recovery of φ after reaching the minimum point also takes place rapidly compared to the non-cooled cases. Notably, in the water-cooled scenarios, a distinct slope change

is observed when φ reaches approximately 35%, which corresponds to the onset of stepwise adsorption behavior in the MIL-101/GO-6 isotherm within the identical relative humidity range (**Figure 4c**). Furthermore, lowering the cooling water temperature causes this slope transition to occur earlier, as seen in the dashed blue line at 283.15 K. When the inlet specific humidity is increased to 20 g/kg$_{DA}$ at 283.15 K, the slope transition occurs even more quickly, as a larger amount of water vapor is supplied to the cooled bed. These findings indicate that maintaining higher bed relative humidity by effectively removing the heat of adsorption is a critical factor for enhancing overall adsorption performance and achieving deep dehumidification.

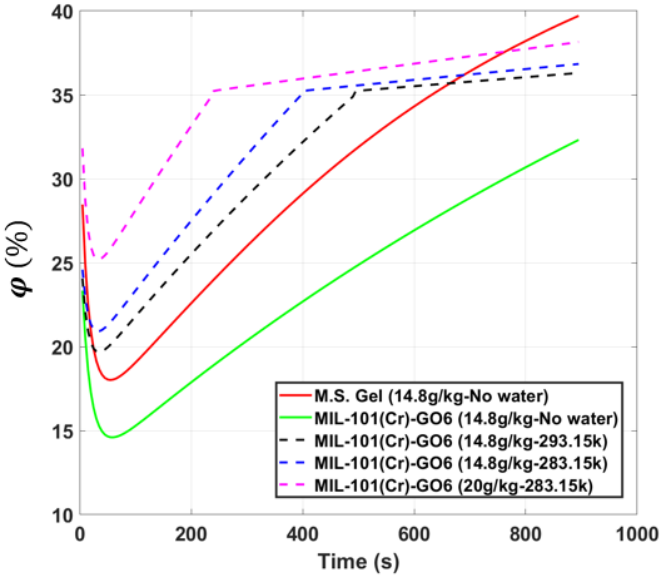

Figure 21. Time course of relative humidity of air in the desiccant bed for M.S. Gel (without internal cooling) and MIL-101/GO-6 (with and without internal cooling). The results show that as the cooling water temperature decreases, φ shifts towards the desired operating window (35 - 47%), where the stepwise adsorption takes place for MIL-101/GO-6.

5.4 Isothermal Dehumidification: Influence of h_{sw} and A_{sw}

As summarized in the previous section, lowering the mean bed temperature through the circulation of chilled water increases the relative humidity of air within the desiccant bed, thereby enhancing overall dehumidification performance. However, reducing the cooling water temperature below 283.15 K is generally impractical, as in most commercial buildings chilled water is supplied within the range 280.15 to 285.15 K. Thus, the two most influential parameters for achieving isothermal dehumidification by suppressing bed temperature rise are the convective heat transfer coefficient between the circulating water and the desiccant bed (h_{sw}), and the available surface area for heat transfer (A_{sw}). Therefore, we conducted a parametric study using MIL-101/GO-6 desiccant, and by varying the magnitudes of h_{sw} and A_{sw}, while maintaining a constant chilled water temperature of 283.15 K to evaluate the influence of altering these parameters on mass adsorbed, mean bed temperature, and bed relative humidity (φ). The results of the parametric study are presented in **Figures 22a–c**, respectively.

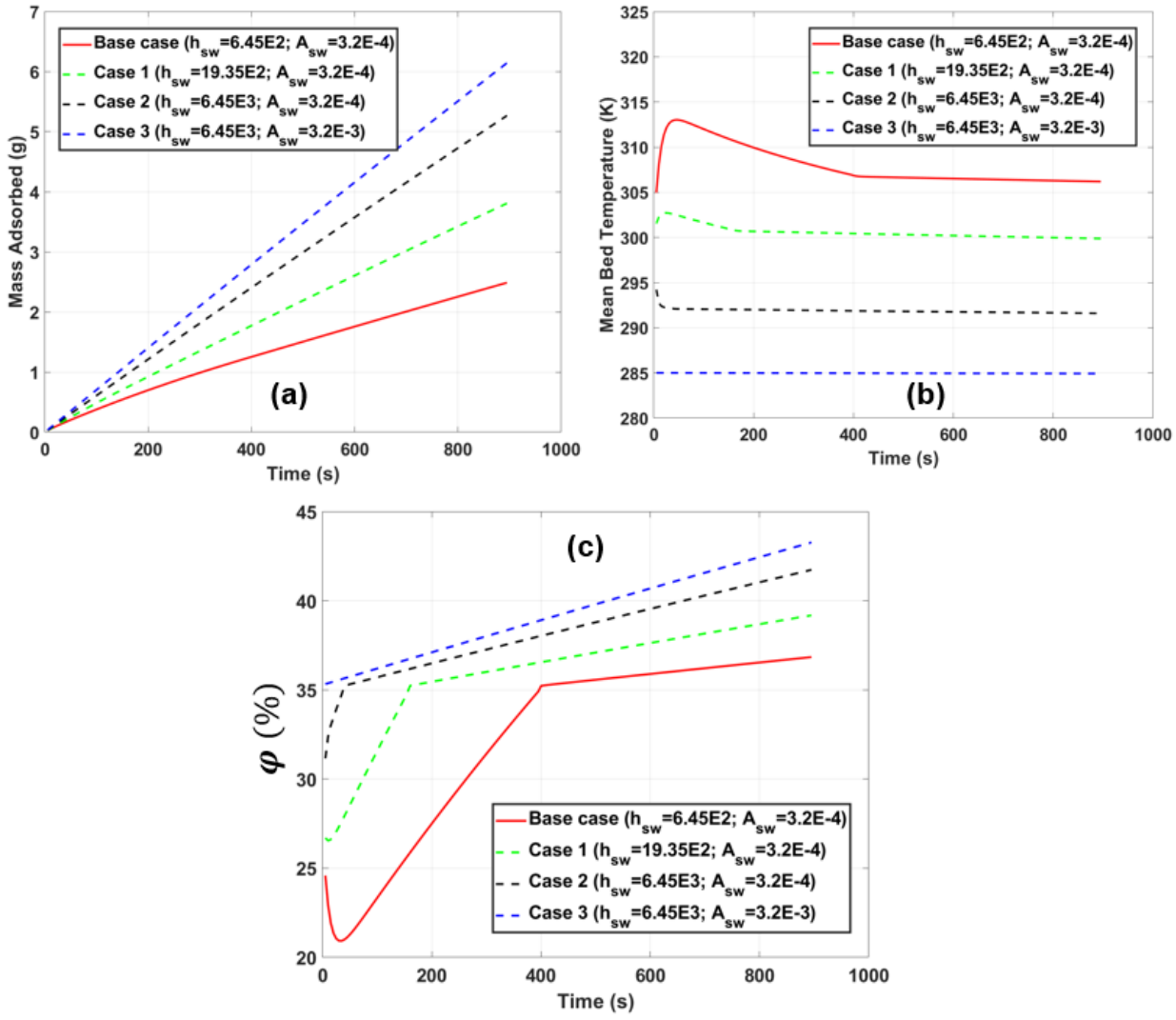

Figure 22. Results of the parametric study showing the influence of heat transfer coefficient (h_{sw}) and heat transfer surface area (A_{sw}) between water and desiccant bed to achieve isothermal dehumidification. Time course of (a) mass adsorbed, (b) mean bed temperature and (c) relative humidity of air within the bed (φ) for increasing values of h_{sw} and A_{sw}. The temperature of cooling water was kept constant at 283.15 K for all cases. The results show that with a ten-fold increment of h_{sw} and A_{sw} the full cooling potential of the chilled water can be utilized, resulting in an isothermal dehumidification.

As shown in **Figure 22a**, hypothetically increasing h_{sw} by fivefold (green dashed lines, Case 1) and tenfold (black dashed lines, Case 2) compared to the baseline case (red solid line), while keeping A_{sw} constant, resulting in a significant enhancement in mass adsorbed. Accordingly, φ also reaches the target operating window (35–47%, corresponding to the stepwise region of the adsorption isotherm in **Figure 4c**) much earlier (**Figure 22c**) as h_{sw} increases. However, in Case 1, the mean bed temperature still exhibits a slight rise during the initial phase of adsorption (**Figure 22b**, green dashed line). In Case 2, the mean bed temperature slightly decreases at the onset of adsorption and then remains nearly constant (**Figure 22b**, black dashed line). Nevertheless, a notable gap between the mean bed temperature and the chilled water

temperature (283.15 K) persists in case 2, indicating that the full cooling potential of the circulating water is not yet fully utilized.

In Case 3, where both h_{sw} and A_{sw} were hypothetically increased by a factor of ten, the mean bed temperature remained nearly constant at approximately 285 K throughout the entire adsorption cycle (blue dashed line in **Figure 22b**), indicating that the cooling potential of the chilled water was fully utilized. Consequently, φ started at 35% and remained within the desired operating window of 35–47% for the whole duration of the adsorption cycle (blue dashed line in **Figure 22c**), which in turn maximized the amount of water adsorbed (blue dashed line in **Figure 22a**). These results clearly demonstrate that achieving isothermal operation of the desiccant bed requires a system design that incorporates internal cooling with both high h_{sw} and enlarged A_{sw}. If the heat exchange between the desiccant bed and the circulating chilled water are inadequate, the benefits of using an advanced desiccant with a step-shape isotherm and high uptake capacity cannot be fully realized. Therefore, enhancing the heat exchange capacity of the desiccant bed is just as critical as improving the desiccant material properties for augmenting overall dehumidification performance. Exploring innovative heat exchanger designs with high surface area—such as triply periodic minimal surfaces, metal foams, and other nature-inspired geometries, including fractal patterns—represents a promising approach in this context.

6 Conclusion

In summary, this study presents a 1D numerical model that solves coupled mass and heat balance equations to predict the mass and heat transfer performance of a previously reported multilayer, binder-free desiccant dehumidifier. The model is validated for both adsorption and regeneration processes using experimental data and CFD results from earlier studies on the M.S. Gel bed without internal cooling. The results demonstrate that the 1D model accurately captures key performance indicators, including mass adsorbed, dehumidification capacity, air temperature change (ΔT_{air}), and mean bed temperature within an acceptable deviation margin compared to experimental and CFD data. The significantly less computational effort required by 1D model as compared to CFD model without sacrificing accuracy makes it a powerful tool for system-level integration, scale-up, and future performance optimization of the MFBDD device using AI-based and data-driven approaches. Upon validation, the model is applied to assess performance enhancements achieved through internal cooling and the use of a step-shape isotherm in a binder-free configuration. The key conclusions from this study are:

- Internal cooling significantly enhances dehumidification performance by lowering the mean bed temperature, thereby maintaining higher relative humidity in the bed and promoting greater water vapor uptake.

- Step-shape adsorption isotherms, such as that of MIL-101/GO-6, enable high working capacity within the narrow relative humidity range (35–47%), but their full potential is realized only when the bed temperature is effectively controlled using circulating chilled water.

- Isothermal operation of the desiccant bed maximizes mass adsorbed and dehumidification capacity by keeping the relative humidity within the target window throughout the adsorption cycle.

- The two most influential parameters to achieve isothermal dehumidification are convective heat transfer coefficient and heat transfer surface area between the desiccant bed and chilled water.

Simultaneously increasing these parameters is essential to fully utilize the cooling potential of the chilled water and maintain an isothermal adsorption cycle.

Lastly, the present study only discusses the dehumidification performance in an internally cooled binder-free dehumidifier and under a wide range of operating conditions. Addressing the demand for chilled water, associated energy consumption and estimating thermal coefficient of performance is beyond the scope of the present study. Therefore, future studies should focus on quantifying these parameters when coupled with a complete HVAC system. Such system-level analysis would enable assessment of the total energy efficiency and operational cost under realistic operating conditions. In addition, optimization of control strategies using machine learning based models—such as dynamic regulation of regeneration temperature, chilled-water flow rate, and cycle timing—could significantly improve energy utilization and system responsiveness. Exploring integration pathways that utilize low-grade waste heat or renewable thermal sources for desiccant regeneration may further enhance the applicability of the MFBDD technology for energy-efficient building climate control systems.

Nomenclature

Symbol	Description	Unit
W	Specific humidity of air	kg/kg_{DA}
W_{avg}	Average specific humidity of air in the air channel	kg/kg_{DA}
T	Temperature	K
t	time	s
u_{air}	Inlet velocity of air	$m\,s^{-1}$
D_{air}	Water diffusivity in the air	$m^2 s^{-1}$
ε_{bed}	Porosity of the bed	-
A_{sheet}	Total cross-sectional area of five desiccant sheets	m^2
A_{ACH}	Total cross-sectional area of the air channels	m^2
ρ_{des}	Density of desiccant	$kg\,m^{-3}$
ρ_{air}	Density of air	$kg\,m^{-3}$
$C_{p,\,air}$	Specific heat capacity of air	$J\,kg^{-1}K^{-1}$
L_{ACH}	Length of air channel	m
Q_{bed}	Adsorbed/desorbed water in the bed	kg/kg_{Des}
Q_{eq}	Adsorbed water at equilibrium	kg/kg_{Des}
$\frac{dQ_{bed}}{dt}$	Adsorption rate	$kg/kg_{Des}/s$
T_{air}	Air temperature	K
α_{air}	Thermal diffusivity of air	$m^2 s^{-1}$
h_{sa}	Convective heat transfer coefficient between air and the bed	$W\,m^{-2}K^{-1}$
A_{sa}	Total heat transfer surface area between air and the bed	m^2
T_w	Water temperature	K
u_w	Inlet velocity of water	$m\,s^{-1}$
α_w	Thermal diffusivity of water	$m^2 s^{-1}$

h_{sw}	Convective heat transfer coefficient between water and the bed	$W\,m^{-2}K^{-1}$
A_{sw}	Total heat transfer surface area between water and the bed	m^2
A_{WCH}	Cross-sectional area of the water channel	m^2
ρ_w	Density of water	$kg\,m^{-3}$
$C_{p,w}$	Specific heat capacity of water	$J\,kg^{-1}K^{-1}$
L_{WCH}	Length of water channel	m
α_{bed}	Thermal diffusivity of the bed	m^2s^{-1}
H_{ads}	Enthalpy of water vapor adsorption	$J\,kg^{-1}$
m_{des}	Mass of desiccant material in bed	kg
m_{bed}	Total mass of the bed	kg
$m_{air\_in\_bed}$	Mass of air in desiccant bed	kg
$C_{p,bed}$	Specific heat capacity of the bed	$J\,kg^{-1}K^{-1}$
$C_{p,des}$	Specific heat capacity of desiccant material	$J\,kg^{-1}K^{-1}$
h_{amb}	Heat loss coefficient to ambient	$W\,K^{-1}$
T_{amb}	Ambient temperature	K
K_{LDF}	LDF rate constant	s^{-1}
a	Langmuir-Sips parameter	-
b_1	Langmuir-Sips parameter	-
b_2	Langmuir-Sips parameter	-
n	Langmuir-Sips parameter	-
φ	Relative Humidity of air in the bed	%
P_{sat}	Saturated partial vapor pressure	Pa
P_v	Partial vapor pressure	Pa
W_{avg}	Average specific humidity of air in the air channel	kg/kg_{DA}
R	Ideal gas constant	$J\,mol^{-1}K^{-1}$
T_{bed}	Temperature of the bed	K
$T_{bed,\,avg}$	Average temperature of the bed	K
M_w	Molar mass of water	$kg\,mol^{-1}$
k_{air}	Thermal conductivity of air	$W\,m^{-2}K^{-1}$
k_{des}	Thermal conductivity of desiccant	$W\,m^{-2}K^{-1}$
k_{bed}	Thermal conductivity of desiccant bed	$W\,m^{-2}K^{-1}$
k_w	Thermal conductivity of water	$W\,m^{-2}K^{-1}$
D_h	Hydraulic diameter of water channel	m
Nu	$Nusselt\ number$	-
Re	$Reynolds\ number$	-
Pr	$Prandtl\ number$	-
μ_w	Dynamic viscosity of water	$Pa\,s$
L_{entry}	Entry length for fully developed flow	m
ϵ_{dehum}	Dehumidification effectiveness	-

Subscripts

$_{DA}$ - Dry air
$_{des}$ - Desiccant
$_{w}$ - Water
$_{ACH}$ - Air Channel
$_{WCH}$ - Water Channel
$_{amb}$ - Ambient
$_{ads}$ - Adsorption
$_{reg}$ - Regeneration
$_{dehum}$ - Dehumidification
$_{LDF}$ - Linear Driving Force
$_{avg}$ - Average
$_{in}$ - Inlet
$_{mid}$ - Middle
$_{out}$ - Outlet
$_{cyc}$ - Cycle

Authors' Contribution

Jubair A. Shamim: Conceptualization, Methodology, Modeling and Simulation, Writing – original draft, review and editing; **Easwaran Krishnan:** Methodology, Writing – original draft, review and editing; **Mingkan Zhang, Lei Gao, Kai Li, Wei-Lun Hsu and Hirofumi Daiguji:** Methodology, Writing – review and editing; **Kashif Nawaz:** Conceptualization, Writing – review & editing, Resources, Project administration, Funding acquisition.

Declaration

The authors declare that they have no known competing financial interests or personal relationships that could have appeared to influence the work reported in this paper.

Acknowledgement

This study was funded by the US Department of Energy (DOE) Office of Energy Efficiency and Renewable Energy (EERE), Building Technologies Office (BTO). This manuscript has been authored by UT-Battelle, LLC, under contract DE-AC05-00OR22725 with the US Department of Energy (DOE). The US Government retains and the publisher, by accepting the article for publication, acknowledges that the US government retains a nonexclusive, paid-up, irrevocable, worldwide license to publish or reproduce the published form of this manuscript or allow others to do so, for the US government purposes. DOE will provide public access to these results of federally sponsored research in accordance with the DOE Public Access Plan (http://energy.gov/downloads/doe-public-access-plan). The authors also acknowledge Katelynn Bearden, Department of Mechanical Engineering, University of Tennessee, Knoxville, USA for checking the language.

References

[1] H. Patel, G. Ge, M.R.H. Abdel-Salam, A.H. Abdel-Salam, R.W. Besant, C.J. Simonson, Contaminant transfer in run-around membrane energy exchangers, Energy and Buildings, 70 (2014) 94-105.
[2] O. Labban, T. Chen, A.F. Ghoniem, J.H. Lienhard, L.K. Norford, Next-generation HVAC: Prospects for and limitations of desiccant and membrane-based dehumidification and cooling, Applied Energy, 200 (2017) 330-346.
[3] R.H. Mohammed, M. Ahmadi, H. Ma, S. Bigham, Desiccants enabling energy-efficient buildings: A review, Renewable and Sustainable Energy Reviews, 183 (2023) 113418.
[4] M.M. Abd-Elhady, M.S. Salem, A.M. Hamed, I.I. El-Sharkawy, Solid desiccant-based dehumidification systems: A critical review on configurations, techniques, and current trends, International Journal of Refrigeration, 133 (2022) 337-352.
[5] D.B. Jani, M. Mishra, P.K. Sahoo, Solid desiccant air conditioning – A state of the art review, Renewable and Sustainable Energy Reviews, 60 (2016) 1451-1469.
[6] V.K. Gorai, S.K. Singh, D.B. Jani, A comprehensive review on solid desiccant-assisted novel dehumidification and its advanced regeneration methods, Journal of Thermal Analysis and Calorimetry, 149 (2024) 8979-9000.
[7] J.A. Shamim, W.-L. Hsu, S. Paul, L. Yu, H. Daiguji, A review of solid desiccant dehumidifiers: Current status and near-term development goals in the context of net zero energy buildings, Renewable and Sustainable Energy Reviews, 137 (2021) 110456.
[8] Y. Ma, S.C. Saha, W. Miller, L. Guan, Comparison of Different Solar-Assisted Air Conditioning Systems for Australian Office Buildings, in: Energies, Vol. 10, 2017.
[9] C.X. Jia, Y.J. Dai, J.Y. Wu, R.Z. Wang, Analysis on a hybrid desiccant air-conditioning system, Applied Thermal Engineering, 26 (2006) 2393-2400.
[10] P. Vivekh, D.T. Bui, M.R. Islam, K. Zaw, K.J. Chua, Experimental performance evaluation of desiccant coated heat exchangers from a combined first and second law of thermodynamics perspective, Energy Conversion and Management, 207 (2020) 112518.
[11] S. Misha, S. Mat, M.H. Ruslan, K. Sopian, Review of solid/liquid desiccant in the drying applications and its regeneration methods, Renewable and Sustainable Energy Reviews, 16 (2012) 4686-4707.
[12] D.B. Jani, Chapter 4 - Performance assessment of solar powered hybrid solid desiccant and dehumidification integrated thermally cooling system using TRNSYS, in: A.K. Azad (ed.) Advances in Clean Energy Technologies, Academic Press, 2021, pp. 171-203.
[13] E.N. Krishnan, H. Ramin, A. Gurubalan, M. Muneeshwaran, K. Li, K. Nawaz, C. Simonson, A methodology for selection of solid desiccants in energy recovery ventilators, Applied Thermal Engineering, 259 (2025) 124830.
[14] J.D. Batukray, Application of Renewable Solar Energy in LiquidDesiccant Powered Dehumidification and Cooling, Journal of Environment Protection and Sustainable Development, 5 (2019) 1-6.
[15] X. Zheng, T.S. Ge, R.Z. Wang, Recent progress on desiccant materials for solid desiccant cooling systems, Energy, 74 (2014) 280-294.
[16] Z. Liu, C. Cheng, J. Han, Z. Zhao, X. Qi, Experimental evaluation of the dehumidification performance of a metal organic framework desiccant wheel, International Journal of Refrigeration, 133 (2022) 157-164.
[17] P. Hou, K. Zu, M. Qin, S. Cui, A novel metal-organic frameworks based humidity pump for indoor moisture control, Building and Environment, 187 (2021) 107396.
[18] K. Yanagita, J. Hwang, J.A. Shamim, W.-L. Hsu, R. Matsuda, A. Endo, J.-J. Delaunay, H. Daiguji, Kinetics of Water Vapor Adsorption and Desorption in MIL-101 Metal–Organic Frameworks, The Journal of Physical Chemistry C, 123 (2019) 387-398.

[19] P. Vivekh, M.R. Islam, K.J. Chua, Experimental performance evaluation of a composite superabsorbent polymer coated heat exchanger based air dehumidification system, Applied Energy, 260 (2020) 114256.
[20] X. Zheng, Y. Zhang, T. Wan, K. Chen, Experimental study on the performance of a novel superabsorbent polymer and activated carbon composite coated heat exchangers, Energy, 281 (2023) 128293.
[21] C.D. Díaz-Marín, L. Masetti, M.A. Roper, K.E. Hector, Y. Zhong, Z. Lu, O.R. Caylan, G. Graeber, J.C. Grossman, Physics-based prediction of moisture-capture properties of hydrogels, Nature Communications, 15 (2024) 8948.
[22] C.T. Wilson, C.D. Díaz-Marín, J.P. Colque, J.P. Mooney, B. El Fil, Solar-driven atmospheric water harvesting in the Atacama Desert through physics-based optimization of a hygroscopic hydrogel device, Device.
[23] K. Nawaz, S.J. Schmidt, A.M. Jacobi, A parametric study on mass diffusion coefficient of desiccants for dehumidification applications: Silica aerogels and silica aerogel coatings on metal foams, Science and Technology for the Built Environment, 21 (2015) 637-647.
[24] U. Puttur, M. Ahmadi, B. Ahmadi, S. Bigham, A novel lung-inspired 3D-printed desiccant-coated heat exchanger for high-performance humidity management in buildings, Energy Conversion and Management, 252 (2022) 115074.
[25] Z. Li, S. Michiyuki, F. Takeshi, Experimental study on heat and mass transfer characteristics for a desiccant-coated fin-tube heat exchanger, International Journal of Heat and Mass Transfer, 89 (2015) 641-651.
[26] J.A. Shamim, G. Auti, H. Kimura, S. Fei, W.-L. Hsu, H. Daiguji, A. Majumdar, Concept of a hybrid compression-adsorption heat pump cycle, Cell Reports Physical Science, 3 (2022).
[27] J.A. Shamim, K. Nawaz, M.-H. Hu, P. Pasqualin, E.N. Krishnan, S.P. Kowalski, P.K. Bhowmik, R. Parameshwaran, W.-L. Hsu, Y. Hwang, H. Daiguji, Review of the potential and challenges of MOF-based adsorption heat pumps for sustainable cooling and heating in the buildings, Energy, 323 (2025) 135846.
[28] J.A. Shamim, W.-L. Hsu, H. Daiguji, Review of component designs for post-COVID-19 HVAC systems: possibilities and challenges, Heliyon, 8 (2022).
[29] Y.H. Feng, Y.J. Dai, R.Z. Wang, T.S. Ge, Insights into desiccant-based internally-cooled dehumidification using porous sorbents: From a modeling viewpoint, Applied Energy, 311 (2022) 118732.
[30] H. Kim, S. Yang, S.R. Rao, S. Narayanan, E.A. Kapustin, H. Furukawa, A.S. Umans, O.M. Yaghi, E.N. Wang, Water harvesting from air with metal-organic frameworks powered by natural sunlight, Science, 356 (2017) 430-434.
[31] B. Zhang, Z. Zhu, X. Wang, X. Liu, F. Kapteijn, Water Adsorption in MOFs: Structures and Applications, Advanced Functional Materials, 34 (2024) 2304788.
[32] S.Z. Shahvari, V.A. Kalkhorani, C.R. Wade, J.D. Clark, Benefits of metal–organic frameworks sorbents for sorbent wheels used in air conditioning systems, Applied Thermal Engineering, 210 (2022) 118407.
[33] A.S. Valarezo, X.Y. Sun, T.S. Ge, Y.J. Dai, R.Z. Wang, Experimental investigation on performance of a novel composite desiccant coated heat exchanger in summer and winter seasons, Energy, 166 (2019) 506-518.
[34] J.D. Chung, D.-Y. Lee, Effect of desiccant isotherm on the performance of desiccant wheel, International Journal of Refrigeration, 32 (2009) 720-726.
[35] J.A. Shamim, X. Liu, E. Krishnan, K. Li, M. Muneeshwaran, H. Jiang, P. Ilani-Kashkouli, K. Nawaz, Advances in Desiccant Wheels for Dehumidification, VOC Mitigation, and CO2 Removal for Energy-Efficient IAQ Management, International Journal of Heat and Mass Transfer, 245 (2025) 126906.
[36] M.M. Abd-Elhady, I.I. El-Sharkawy, A.M. Hamed, M.S. Salem, Transient mass and heat transport modeling in a multi-tray packed bed solid desiccant dehumidifier: A parametric analysis, International Journal of Refrigeration, 157 (2024) 109-117.

[37] S. De Antonellis, L. Colombo, A. Freni, C. Joppolo, Feasibility study of a desiccant packed bed system for air humidification, Energy, 214 (2021) 119002.
[38] Y.-C. Chiang, C.-H. Chen, Y.-C. Chiang, S.-L. Chen, Circulating inclined fluidized beds with application for desiccant dehumidification systems, Applied Energy, 175 (2016) 199-211.
[39] L.M. Hu, T.S. Ge, Y. Jiang, R.Z. Wang, Performance study on composite desiccant material coated fin-tube heat exchangers, International Journal of Heat and Mass Transfer, 90 (2015) 109-120.
[40] J. Liu, C. Sun, Q. Chen, Experimental study of desiccant-coated heat exchangers for deep dehumidification, Energy and Buildings, 319 (2024) 114554.
[41] M.Z. Liu, W.D. Chen, Y.L. Shao, Z.F. Huang, Z.Y. Zeng, Y.D. Wan, K.J. Chua, Experimental analysis and investigation of desiccant coated heat exchanger applications involving condensation and sorption mechanisms, Energy, 305 (2024) 132255.
[42] X.Y. Sun, Y.J. Dai, T.S. Ge, Y. Zhao, R.Z. Wang, Experimental and comparison study on heat and moisture transfer characteristics of desiccant coated heat exchanger with variable structure sizes, Applied Thermal Engineering, 137 (2018) 32-46.
[43] X. Lei, W. Ying, Z. Xue, H. Zhang, J. Wang, A novel curdlan based desiccant coated heat exchanger for efficient dehumidification, Scientific Reports, 15 (2025) 7404.
[44] X. Zhou, M. Goldsworthy, A. Sproul, Performance investigation of an internally cooled desiccant wheel, Applied Energy, 224 (2018) 382-397.
[45] W. Yang, J. Ren, Z. Lin, Z. Wang, X. Zhao, Study on Dehumidification Performance of a Multi-Stage Internal Cooling Solid Desiccant Adsorption Packed Bed, in: Energies, Vol. 11, 2018.
[46] T.U. Erkek, A. Gungor, H. Fugmann, A. Morgenstern, C. Bongs, Performance evaluation of a desiccant coated heat exchanger with two different desiccant materials, Applied Thermal Engineering, 143 (2018) 701-710.
[47] C. Wang, X. Ji, B. Yang, R. Zhang, D. Yang, Study on heat transfer and dehumidification performance of desiccant coated microchannel heat exchanger, Applied Thermal Engineering, 192 (2021) 116913.
[48] Q.W. Pan, Y.L. Ruan, X.Y. Li, Q.Y. Zhao, B. Wang, Z.H. Gan, Performance assessment of heat exchanger coated with encapsulated ultra-high salt content desiccant, Applied Thermal Engineering, 231 (2023) 120974.
[49] Z. Hua, S. Cai, H. Xu, W. Yuan, S. Li, Z. Tu, Investigations of Silica/MOF composite coating and its dehumidification performance on a desiccant-coated heat exchanger, Energy, 307 (2024) 132576.
[50] L. Ge, Y. Feng, J. Wu, R. Wang, T. Ge, Performance evaluation of MIL-101(Cr) based desiccant-coated heat exchangers for efficient dehumidification, Energy, 289 (2024) 130049.
[51] G.A. Shaik, V. Prabakaran, M.K. Jagirdar, Experimental investigation on a novel, counter flow solid desiccant-coated fin tube heat exchanger driven by ultra-low-grade-heat source in humid conditions, Applied Thermal Engineering, 279 (2025) 127624.
[52] V.R. Abishraj, G. Annadurai, C. Simonson, M.P. Maiya, Performance evaluation of wavy fin desiccant coated heat exchanger for hot and humid climatic conditions, Applied Thermal Engineering, 245 (2024) 122741.
[53] P. Vivekh, M. Kumja, D.T. Bui, K.J. Chua, Recent developments in solid desiccant coated heat exchangers – A review, Applied Energy, 229 (2018) 778-803.
[54] T. Venegas, M. Qu, K. Nawaz, L. Wang, Critical review and future prospects for desiccant coated heat exchangers: Materials, design, and manufacturing, Renewable and Sustainable Energy Reviews, 151 (2021) 111531.
[55] J.A. Shamim, W.-L. Hsu, K. Kitaoka, S. Paul, H. Daiguji, Design and performance evaluation of a multilayer fixed-bed binder-free desiccant dehumidifier for hybrid air-conditioning systems: Part I – experimental, International Journal of Heat and Mass Transfer, 116 (2018) 1361-1369.
[56] W.-L. Hsu, S. Paul, J.A. Shamim, K. Kitaoka, H. Daiguji, Design and performance evaluation of a multilayer fixed-bed binder-free desiccant dehumidifier for hybrid air-conditioning systems: Part II – Theoretical analysis, International Journal of Heat and Mass Transfer, 116 (2018) 1370-1378.

[57] J.A. Shamim, S. Paul, K. Kitaoka, W.-L. Hsu, H. Daiguji, Experimental evaluation of transient heat and mass transfer during regeneration in multilayer fixed-bed binder-free desiccant dehumidifier, International Journal of Heat and Mass Transfer, 128 (2019) 623-633.
[58] J.A. Shamim, S. Paul, W.-L. Hsu, K. Kitaoka, H. Daiguji, Theoretical analysis of transient heat and mass transfer during regeneration in multilayer fixed-bed binder-free desiccant dehumidifier: Model validation and parametric study, International Journal of Heat and Mass Transfer, 134 (2019) 1024-1040.
[59] Mesh Corporation, Japan (https://www.mesh.co.jp/seihin/screen_mesh_E.html); accessed 05.15.2025, in.
[60] RESIFA™ M.S.GEL Particles for Chromatography Materials (https://www.agcchem.com/products/fine-silica-gels-2/fine-silica-products-for-chromatography/#technical-documents); accessed 05.15.2025, in.
[61] L. Yu, J.A. Shamim, W.-L. Hsu, H. Daiguji, Optimization of parameters for air dehumidification systems including multilayer fixed-bed binder-free desiccant dehumidifier, International Journal of Heat and Mass Transfer, 172 (2021) 121102.
[62] J. Yan, Y. Yu, C. Ma, J. Xiao, Q. Xia, Y. Li, Z. Li, Adsorption isotherms and kinetics of water vapor on novel adsorbents MIL-101(Cr)@GO with super-high capacity, Applied Thermal Engineering, 84 (2015) 118-125.
[63] J. Zhao, X. Li, C. Shum, J. McPhee, A Review of physics-based and data-driven models for real-time control of polymer electrolyte membrane fuel cells, Energy and AI, 6 (2021) 100114.
[64] J.W. Lee, W.G. Shim, H. Moon, Adsorption equilibrium and kinetics for capillary condensation of trichloroethylene on MCM-41 and MCM-48, Microporous and Mesoporous Materials, 73 (2004) 109-119.
[65] Y. Yan, S.C. King, M. Li, T. Galy, M. Marszewski, J.S. Kang, L. Pilon, Y. Hu, S.H. Tolbert, Exploring the Effect of Porous Structure on Thermal Conductivity in Templated Mesoporous Silica Films, The Journal of Physical Chemistry C, 123 (2019) 21721-21730.
[66] X. Xia, S. Li, Improved adsorption cooling performance of MIL-101(Cr)/GO composites by tuning the water adsorption rate, Sustainable Energy & Fuels, 7 (2023) 437-447.
[67] E. Elsayed, H. Wang, P.A. Anderson, R. Al-Dadah, S. Mahmoud, H. Navarro, Y. Ding, J. Bowen, Development of MIL-101(Cr)/GrO composites for adsorption heat pump applications, Microporous and Mesoporous Materials, 244 (2017) 180-191.
[68] M.G.V. Wee, A. Chinnappan, R. Shang, P.S. Lee, S. Ramakrishna, Enhanced moisture sorption through regulated MIL-101(Cr) synthesis and its integration onto heat exchangers, Journal of Materials Chemistry A, 12 (2024) 824-839.
[69] Water Density, Specific Weight and Thermal Expansion Coefficients - Temperature and Pressure Dependence (https://www.engineeringtoolbox.com/water-density-specific-weight-d_595.html); accessed 05.08.2025, in.
[70] S. Sircar, J.R. Hufton, Why Does the Linear Driving Force Model for Adsorption Kinetics Work?, Adsorption, 6 (2000) 137-147.
[71] Water - Dynamic and Kinematic Viscosity at Various Temperatures and Pressures (https://www.engineeringtoolbox.com/water-dynamic-kinematic-viscosity-d_596.html); accessed 05.08.2025, in.
[72] H.S. Lee, C.J. Matthews, R.D. Braddock, G.C. Sander, F. Gandola, A MATLAB method of lines template for transport equations, Environmental Modelling & Software, 19 (2004) 603-614.
[73] B. Han, A. Chakraborty, Recent advances in metal-organic frameworks for adsorption heat transformations, Renewable and Sustainable Energy Reviews, 198 (2024) 114411.
[74] M.H. Bagheri, S.N. Schiffres, Ideal Adsorption Isotherm Behavior for Cooling Applications, Langmuir, 34 (2018) 1908-1915.
[75] J. Canivet, A. Fateeva, Y. Guo, B. Coasne, D. Farrusseng, Water adsorption in MOFs: fundamentals and applications, Chemical Society Reviews, 43 (2014) 5594-5617.